Postprint of: Winczewski Sz., Rybicki J., Anisotropic mechanical behavior and auxeticity of penta-graphene: Molecular statics/molecular dynamics studies, Carbon, Vol. 146 (2019), pp 572-587, DOI: 10.1016/j.carbon.2019.02.042

Anisotropic mechanical behavior and auxeticity of penta-graphene: molecular statics/molecular dynamics studies

Szymon Winczewski[a,*], Jarosław Rybicki[a,b]

[a] *Faculty of Applied Physics and Mathematics, Gdansk University of Technology, Narutowicza 11/12, 80-233 Gdańsk, Poland.*
[b] *TASK Computer Centre, Gdansk University of Technology, Narutowicza 11/12, 80-233 Gdańsk, Poland*

Abstract

We investigate the mechanical properties of penta-graphene (PG), a recently proposed two-dimensional carbon allotrope using atomistic simulation techniques combined with the empirical description of interatomic interactions. We report on the dependence of its three in-plane mechanical moduli (*i.e.* Young's modulus, Poisson's ratio and shear modulus) on the deformation direction, strain and temperature. We show that PG displays a strongly manifested mechanical anisotropy, being characterized by Poisson's ratio and the shear modulus which both depend strongly on the deformation direction. By analyzing bond energies we study the influence of different carbon-carbon bonds on the mechanical response of PG and based on that we explain the origins of the observed anisotropy. We show that it is mostly a consequence of the characteristics of the sp^3-hybridizied bonds, which form the diamond-like tetrahedral blocks. We investigate the auxeticity of PG in detail and show that it displays complete auxetic behavior, having negative Poisson's ratio for all the deformation directions. We show that the auxeticity of PG is similar to that of defective graphene containing 5-8-5 double vacancies, as it also originates from the so-called de-wrinkling mechanism. We study the influence of temperature and show that it only slightly affects the mechanical moduli of PG.

*Corresponding author
Email address: szymon.winczewski@pg.edu.pl (Szymon Winczewski)

1. Introduction

Penta-graphene (PG) is a new carbon allotrope, which has been proposed theoretically based on *ab initio* calculations [1]. Similarly to graphene, PG is a two-dimensional crystal, however, its structure is completely made of pentagons.

Since its discovery, PG has been gaining much interest [2–23], mostly because of its electric properties. As opposed to graphene, PG possesses a band gap, which presence makes PG a good candidate material for two-dimensional transistors. Furthermore, its electric properties can be fine-tuned by functionalization [6, 8], doping [6, 22] or by applying stacking [5, 12]. This further stimulates interest in this structure.

PG is also interesting because of its unique mechanical properties. It has very high in-plane stiffness, which reaches 265 GPa nm [1], *i.e.* more than two thirds of that of graphene. In addition, it is also characterized by very high mechanical strength, being able to withstand strains as high as 25% [1]. PG has also another interesting mechanical property. Having a negative Poisson's ratio it belongs to the group of materials called auxetics, which expand in the transverse direction during stretching.

Insofar the electrical properties of PG are already well known, its mechanical properties have not been a subject of intensive research. In addition to the original work of Zhang *et al.* [1], which presented the linear elastic constants of PG, the mechanical properties of PG have been investigated – to our best knowledge – in three other papers [7, 11, 17] only.

In Ref. [11] Sun *et al.* focused on nonlinear mechanical properties of PG and studied its behavior at large deformations by using density functional theory (DFT) calculations combined with the fourth order continuum elasticity theory. They also made an attempt to explain the auxeticity of PG, concluding that it results from a de-wrinkling mechanism. Despite such a significant expansion of knowledge, Ref. [11] did not present a complete picture of the variability of mechanical properties of PG, because the problem of their dependence on the direction was not raised.

The mechanical properties of PG were also investigated by Le [17], who stud-

ied the influence of temperature on Young's modulus and the yield point of PG. However, Le's studies did not provide any insight into the anisotropy of the mechanical properties of PG either, as he limited his studies to only one family of crystallographic directions, namely ⟨100⟩. What is more important, the credibility of his results can be questioned by the fact that in his studies he applied the REAX potential [24], which in our recent work [25] we found as rather inappropriate for describing PG. A similar – and in our opinion inappropriate – approach was applied by Cranford in Ref. [7], who also used the REAX potential [24] to study the mechanical behavior of finite (hydrogen-terminated) PG sheets during uniaxial tension. His studies did not give an insight into the mechanical anisotropy of PG either, as he also considered only one deformation direction, namely [110].

It is worth noting that the way in which PG is built, especially the fact that it is made of non-equivalent sp^2- and sp^3-hybridizied atoms, which – in addition – form a very untypical lattice, spanned by bonds of different stiffness and orientations, suggests a potentially strong dependence of its mechanical properties on direction. However, a comprehensive description of these properties is still missing in the literature. It is also still unclear how the interplay between non-equivalent bonds present in PG builds its mechanical response, and how this picture changes when deformation is carried out in different directions.

In the present work we made an attempt to fill the above mentioned gaps. We investigated the mechanical properties of PG and completely described its in-plane mechanical response by using molecular statics (MS) and molecular dynamics (MD) simulations combined with the empirical description of interatomic interactions. We also performed a detailed bond energy analysis and analysis of the geometry changes and based on that we explained the origins of the observed mechanical anisotropy. We also characterized the influence of temperature on the mechanical properties of PG.

This work is organized as follows. In Section 2 we recap the basic information about PG and present the methodology used. In Section 3 we present the results of MS calculations of the mechanical properties of PG at zero temperature. In Section 4 we explain the observed mechanical anisotropy, relating the obtained picture to

the features of the PG structure and the specifics of its bonding. In Section 5 we investigate the influence of temperature on the mechanical properties of PG, presenting the results of MD simulations. Section 6 is a summary.

2. Penta-graphene

2.1. Structure

The structure of PG (as described by Zhang *et al.* in [1]) is presented in Figure 1. PG belongs to the tetragonal space group P-42_1m with the lattice parameters $a = b = 3.64$ Å and it has a layered structure (see Figure 1b) made of two types of carbon atoms. The middle layer (with $z = 0$) contains only sp^3-hybridizied atoms (later on termed as C1 atoms), while the upper and lower layers (with $z = \pm h$) contain only sp^2-hybridizied atoms (detoned as C2). Here, h denotes the interlayer spacing which – according to Ref. [1] – equals 0.6 Å. The carbon-carbon bonds have the lengths $d_1 = 1.55$ Å (all C1-C2 bonds) and $d_2 = 1.34$ Å (all C2-C2 bonds).

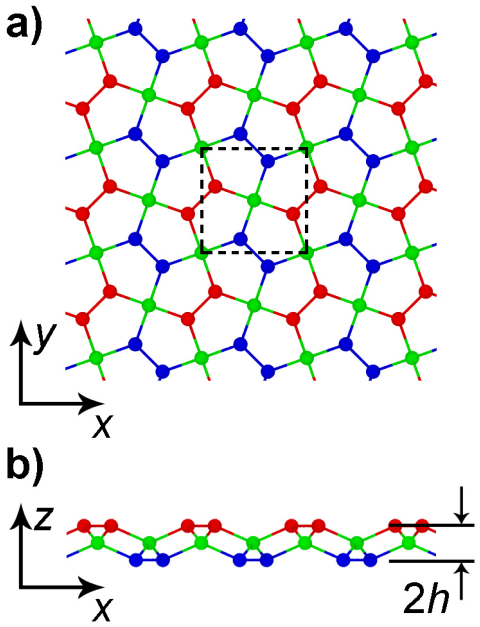

Figure 1: Structure of penta-graphene: top (panel a) and side (panel b) views. The sp^3-hybridizied atoms (C1) are shown in green, while the sp^2-hybridizied atoms (C2) are shown in blue (lower layer with $z = -h$) and red (upper layer with $z = +h$). The illustration was prepared using OVITO [26].

PG forms a structure which is similar to the Cairo pentagonal tiling (CPT). Similarly to CPT, all pentagons in PG are the same. However, their geometry differs slightly from that seen in CPT. This originates from the fact that PG is not strictly planar, while CPT is. In CPT the interior angles of pentagons are equal to 120 (occurs three times) and 90 degrees (occurs twice), while in PG the corresponding angles are equal to 113.5 (C1-C2-C2 angle, occurs twice), 112.4 (C1-C2-C1 angle) and $\alpha = 98.6$ degrees (C2-C1-C2 angle, also occurs twice). There is also another C2-C1-C2 angle, which measures the corrugation of the PG structure. According to Ref. [1] it is equal to $\beta = 134.4$ degrees.

2.2. Mechanical properties

The presence of strong covalent bonds is the reason why PG has very high stiffness, with the corresponding Young's modulus equal to $E = 264$ GPa nm. PG is also characterized by a high shear modulus $\mu = 152$ GPa nm and a negative Poisson's ratio $\nu = -0.068$. The above presented values of moduli are taken from Ref. [1] and correspond to the $\langle 100 \rangle$ family of directions. In this work we will focus on the anisotropy of mechanical properties, with the main scope being to determine the dependence of the mechanical moduli E, ν and μ on the deformation direction and strain.

To describe the deformation direction we will use the angle θ, which we define as the angle between the deformation direction and the crystallographic direction [100]. Therefore $\theta = \pi/4$ will correspond to the [110] direction, while $\theta = \pi/2$ will correspond to the [010] direction.

The symmetry of PG is the reason why the range of the considered directions (angles θ) can be restricted to $\theta \in [0, \pi/4]$. For larger angles the following relations can be used:

$$P(\pi/4 + \theta) = P(\pi/4 - \theta), \qquad \text{for } \theta \in (0, \pi/4], \tag{1}$$

$$P(\pi/2 + \theta) = P(\theta), \qquad \text{for } \theta \in (0, \pi/2], \tag{2}$$

$$P(\pi + \theta) = P(\theta), \qquad \text{for } \theta \in (0, \pi). \tag{3}$$

in order to obtain the value of mechanical modulus P (where $P = E, \nu$ or μ) for any angle θ.

Throughout this work we will use the Voigt notation. The axial and transverse directions will always correspond to the x and y directions, respectively, and the corresponding strains will be denoted with ε_1 and ε_2 symbols, respectively. The shear strain will be denoted as ε_6. Consequently, the corresponding elements of the stress tensor will be denoted with σ_1, σ_2 and σ_6 symbols. Stresses will be expressed in units of GPa nm (which equals N/m), *i.e.* as a linear force density. This unit is much more convenient for the description of single layer thick systems, as it does not necessitate defining the thickness of the considered structure, which is often problematic and may cause some ambiguities.

2.3. Interatomic interactions

Penta-graphene constitutes a challenging system for the empirical potentials. This mostly originates from its mixed sp^2-sp^3 hybridization but is also a consequence of the fact, that the base structural building blocks of PG differ strongly from their counterparts seen in diamond and graphite/graphene.

In our previous work [25] we showed that among empirical potentials available for the elemental carbon there is only one potential which correctly describes all the important features of PG. It is a parameterization of the Tersoff potential [27, 28] proposed in 2005 by Erhart and Albe [29]. As we showed in Ref. [25], this potential reproduces very well the structure of PG and its linear mechanical properties (in Table 1 we compare the properties obtained with this potential with the DFT results of Ref. [1]). At the same time it provides a reliable picture of the thermodynamic stability of PG. This potential also satisfactorily (as for an empirical model) describes the nonlinear mechanical behavior of PG, even at strains as high as 0.2. This further justifies its application in studies on the anisotropy of the mechanical properties of PG, allowing us to believe that the obtained picture will be qualitatively true and quantitatively satisfactory. Therefore, in this work we have employed this potential to describe the interactions of carbon atoms in PG.

Table 1: Structural and mechanical properties of the penta-graphene obtained with the DFT method [1] compared with the empirical calculations [25] based on the parameterization of the Tersoff potential proposed by Erhart and Albe [29]. C_{11}, C_{12} and C_{66} symbols denote the elastic constants, while ϕ denotes the so-called deflection angle (for details, please see Ref. [22]). In the last column we present the signed relative error, which was calculated by taking the DFT results as the reference.

Property	DFT	Tersoff potential	Relative error (%)
Structural			
$a = b$ (Å)	3.64	3.59	-1.4
h (Å)	0.60	0.71	18
d_1 (Å)	1.55	1.55	-0.25
d_2 (Å)	1.34	1.48	11
α (degrees)	98.6	102	3.4
β (degrees)	134.2	125.7	-6.4
ϕ (degrees)	19.17	24.11	26
Mechanical			
C_{11} (GPa nm)	265	244	-7.9
C_{12} (GPa nm)	-18.0	-20.6	15
$C_{66} = \mu$ (GPa nm)	152	162	6.7
E (GPa nm)	264	242	-8.1
ν	-0.068	-0.085	24

The total potential energy U_{tot} of the system composed of N atoms within the Tersoff potential is given by:

$$U_{\mathrm{tot}} = \sum_i \sum_{j>i} f_{\mathrm{C}}(r_{ij}) \left[V_{\mathrm{R}}(r_{ij}) - \frac{b_{ij} + b_{ji}}{2} V_{\mathrm{A}}(r_{ij}) \right] = \sum_i \sum_{j>i} V_{ij}. \tag{4}$$

Here, r_{ij} denotes the distance between atoms i and j. The functions $V_{\mathrm{R}}(r)$ and $V_{\mathrm{A}}(r)$ describe repulsion and attraction and both have an exponential form. The factor $\overline{b}_{ij} = (b_{ij} + b_{ji})/2$ which occurs before the second term is the so-called bond order. By scaling the attractive term V_{A} it controls the strength of the bond, enabling a simultaneous (*i.e.* obtained within one approach) description of single, double

and triple covalent bonds. The $\overline{b}_{ij}$ parameter depends in the nonlinear way on the configuration of the system in the vicinity of atoms i and j. This causes the Tersoff potential to be, in fact, a many-body potential.

The cutoff function $f_{\mathrm{C}}(r)$ smoothly turns off the interactions between distant atoms, causing that it is only the contributions of pairs of atoms which are covalently bonded that are included in the double summation present in Eq. (4). Thus, it is possible to consider the V_{ij} contribution to be energy associated with the i-j bond. However, it must stressed here that the V_{ij} contribution defined in this way is not a two body contribution, as it depends also on the positions of atoms which are nearest neighbors of atoms i and j, through the bond order $\overline{b}_{ij}$. In fact, the V_{ij} term describes not only the energetics of the bond stretching, but also captures all the bond-bond effects that occur when the valence angle between two adjacent bonds is varied. In this work we do not present a detailed description of the underlying physics. However, we emphasize the importance of the rightmost form of Eq. (4), which we will use later in this work.

3. Mechanical properties at zero temperature

3.1. Simulation protocol

At the beginning we examined the mechanical response of PG at zero temperature, neglecting – but only for now – the influence of temperature. In the calculations for zero temperature we used the molecular statics method. All the calculations presented in this work were carried out using the LAMMPS simulation package [30] in a monoclinic simulation box spanned by vectors $\mathbf{A} = [L_x, 0, 0]$, $\mathbf{B} = [X_y, L_y, 0]$ and $\mathbf{C} = [0, 0, L_z]$. The penta-graphene was laying in the xy plane with the periodic boundary conditions (PBC) applied in the x and y coordinate directions. The crystal lattice of PG was oriented in such a way that the chosen deformation direction was aligned with the x axis. The simulations were carried out for systems consisting of 2400 up to 3576 atoms, depending on the chosen deformation direction.

We considered 42 different deformation directions from the range $\theta \in [0, \pi/4]$. For each direction θ the calculations started with the equilibrium structure obtained

from the energy minimization (details regarding the procedure employed for minimization can be found in Ref. [25], the initial structure used in this work corresponds to the global minimum identified there). The equilibrated (i.e. corresponding to the zero strain) structure was then deformed by incrementally dilating the simulation box along the loading direction and applying an equal affine transformation to the atomic positions. This was followed by the energy minimization of the atomic coordinates. The minimization was carried out using the Polak-Ribiére [31] formulation of the conjugate gradient method. Strict convergence criteria were always used. The termination criterion for all the atomic force components was to be below 10^{-8} eV Å^{-1}, with the final positions being accurate to no worse than 10^{-6} Å.

To determine all the three in-plane moduli (E, ν and μ) we considered two deformation types: uniaxial stretching and simple shearing. In the case of uniaxial stretching, for each considered state (defined by ε_1) the L_y and X_y coordinates of the simulation box were also optimized during the minimization procedure, to ensure that the obtained state was truly characterized by $\sigma_2 = \sigma_6 = 0$ (with $\sigma_1 \neq 0$). For this deformation type we considered 201 different strains in the range $\varepsilon_1 \in [0, 0.2]$. In the case of simple shearing, the L_x and L_y simulation box sizes were relaxed, in order to obtain a state characterized by $\sigma_1 = \sigma_2 = 0$ (with $\sigma_6 \neq 0$). For this deformation type we considered 101 different strains in the range $\varepsilon_6 \in [0, 0.1]$. Knowing the sizes of the deformed system (*i.e.* L_x, L_y and X_y), the axial and the transverse strains were calculated as $\varepsilon_1 = (L_x - L_x^0)/L_x^0$ and $\varepsilon_2 = (L_y - L_y^0)/L_y^0$, respectively, while the shear strain was calculated as $\varepsilon_6 = X_y/L_y^0$. Here, L_x^0 and L_y^0 represent the sizes of the undeformed system.

3.2. Results

We start the presentation with the results corresponding to the uniaxial stretching. The stress-strain $\sigma_1(\varepsilon_1)$ dependencies obtained for four exemplary directions (*i.e.* $\theta = 0, \pi/12, \pi/6$ and $\pi/4$) are presented in Figure 2a. On their basis we determined the strain dependent Young's modulus $E(\varepsilon_1)$, defined by:

$$E(\varepsilon_1) = \frac{\partial \sigma_1(\varepsilon_1)}{\partial \varepsilon_1}, \tag{5}$$

which was found by differentiating the sixth degree polynomial fitted to the $\sigma_1(\varepsilon_1)$ data. The obtained $E(\varepsilon_1)$ curves are presented in Figure 2b.

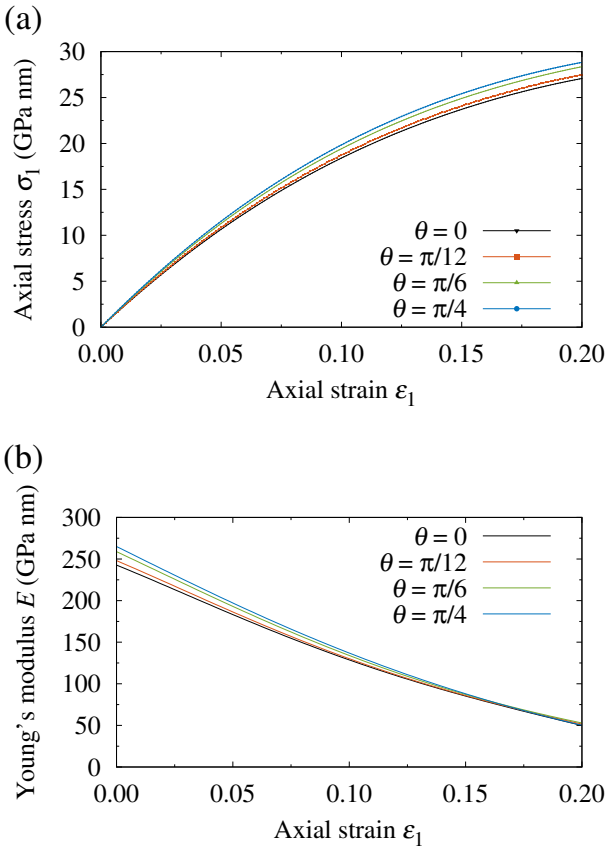

Figure 2: Uniaxial stretching of penta-graphene: strain-stress curves (panel a) and strain dependent Young's modulus (panel b). The solid lines on panel a represent polynomial fits (see text).

Even the first glance shows that the mechanical response of PG is characterized by strong nonlinearity. For all directions a continuous decrease in the strain dependent Young's modulus $E(\varepsilon_1)$ is observed. As a result at $\varepsilon_1 = 0.1$ and $\varepsilon_1 = 0.2$ strain E decreases to about 50% and 20% of its initial value, respectively. The anisotropy of the mechanical properties is also visible. The highest stiffness is observed for $\theta = \pi/4$, for which we obtained $E(\varepsilon_1 = 0) = 265$ GPa nm, which is by about 10% higher than the value obtained for $\theta = 0$. In Figure 5a we present a 2D map which shows how Young's modulus E depends on ε_1 for all the studied deformation directions θ.

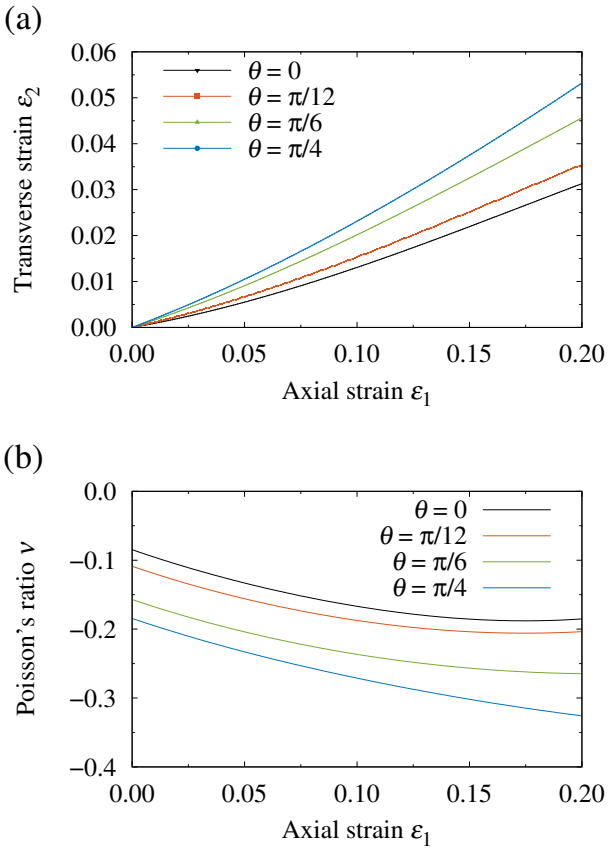

Figure 3: Uniaxial stretching of penta-graphene: strain-strain curves (panel a) and strain dependent Poisson's ratio (panel b). The solid lines on panel a represent polynomial fits (see text).

A strong nonlinearity is also observed on the $\varepsilon_2(\varepsilon_1)$ curves (Figure 3a). This can be easily seen by analyzing the strain dependent Poisson's ratio $\nu(\varepsilon_1)$ (see Figure 3b), defined by:

$$\nu(\varepsilon_1) = -\frac{\partial \varepsilon_2(\varepsilon_1)}{\partial \varepsilon_1} \tag{6}$$

and found in a way analogous to $E(\varepsilon_1)$ (sixth degree polynomial was used to approximate the $\varepsilon_2(\varepsilon_1)$ data and then differentiated).

Our calculations have shown that for all directions the Poisson's ratio decreases strongly with the increasing axial strain ε_1. For $\theta = 0$ the initial (*i.e.* zero strain) Poisson's ratio was found as $\nu(\varepsilon_1 = 0) = -0.085$, while for the highest studied strain (and the same direction) we obtained $\nu(\varepsilon_1 = 0.2) = -0.185$, which gives more than a two-fold change in the absolute value of ν. For $\theta = \pi/4$ this ratio turned out to

be only slightly lower (≈ 1.75).

In the case of the Poisson's ratio the mechanical anisotropy manifests itself even stronger than in the case of Young's modulus. This is clearly visible when one compares the ratio of extreme Poisson's ratios, which was found as

$$\frac{\nu(\varepsilon_1 = 0, \theta = \pi/4)}{\nu(\varepsilon_1 = 0, \theta = 0)} \approx 2.2. \tag{7}$$

Poisson's ratio decreases monotonically with increasing θ and ε_1. The only slight deviation from this character is observed for directions $\theta \in [0, \pi/12]$ and strains $\varepsilon_1 \in [0.15, 0.20]$. This is clearly visible on a 2D map of $\nu(\theta, \varepsilon_1)$ shown in Figure 5b, which presents the behavior of ν in the entire studied region. It is worth noting that Poisson's ratio turned out to be negative for all the studied directions (and all the studied strains). This property, which is often termed as complete auxeticity, is very rare.

Now we will discuss the results corresponding to the shearing. In Figure 4a we present four examples of $\sigma_6(\varepsilon_6)$ dependencies. Based on them we calculated the strain dependent shear modulus:

$$\mu(\varepsilon_6) = \frac{\partial \sigma_6(\varepsilon_6)}{\partial \varepsilon_6}, \tag{8}$$

which was calculated in a way analogous to that used previously. The obtained $\mu(\varepsilon_6)$ dependencies are presented in Figure 4b.

The anisotropy of the shear modulus is also clearly visible. Its value strongly depends on the deformation direction and is the lowest for $\theta = \pi/4$. For this direction and the zero strain we obtained $\mu(\varepsilon_6 = 0) = 132.6$ GPa nm, which is by 20% lower than the value obtained for $\theta = 0$ (162.5 GPa nm), for which PG systematically (*i.e.* for all studied strains) displays the highest rigidity.

The dependence of the shear modulus on θ and ε_6 turned out to be very similar to that of Poisson's ratio. This is clearly visible when the contour plots of μ (Figure 5c) and ν (Figure 5b) are compared. In both cases the highest value of the modulus was obtained for $\theta = 0$ and the zero strain, while the lowest value was found for $\theta = \pi/4$ and the highest strain. This observation suggests that the mechanism of PG auxeticity must be somehow related to the mechanism which "builds up" its rigidity. We will address this issue later in this work.

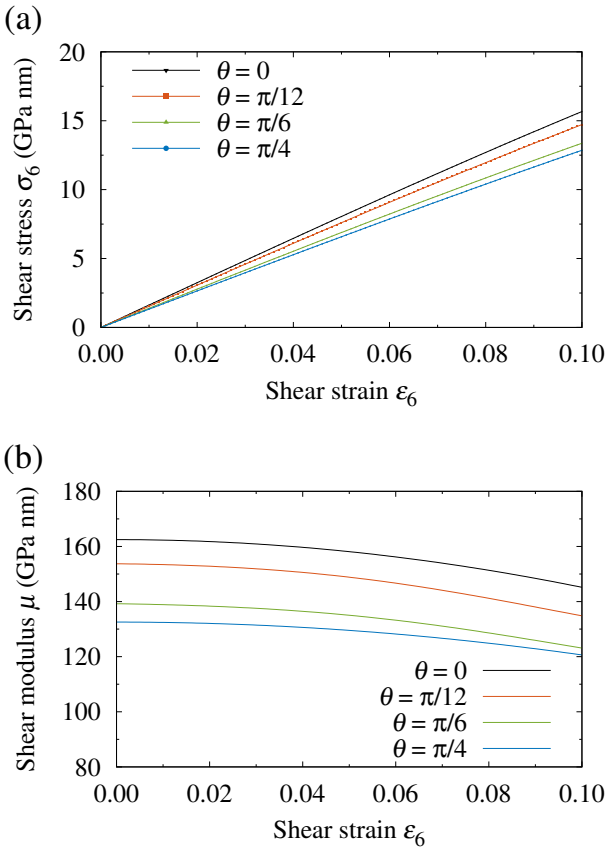

Figure 4: Simple shearing of penta-graphene: strain-strain curves (panel a) and strain dependent shear modulus (panel b). The solid lines on panel a represent polynomial fits (see text).

In order to facilitate the use of our results (*e.g.* in continuum modeling) we have described the obtained dependencies of mechanical moduli E, ν and μ with 2D polynomials of the form:

$$\begin{aligned} f(\theta,\varepsilon) &= a_{0,0} + a_{1,0}\theta + a_{0,1}\varepsilon + a_{2,0}\theta^2 + a_{1,1}\theta\varepsilon + a_{0,2}\varepsilon^2 + \\ &\quad a_{3,0}\theta^3 + a_{2,1}\theta^2\varepsilon + a_{1,2}\theta\varepsilon^2 + a_{0,3}\varepsilon^3 + \\ &\quad a_{4,0}\theta^4 + a_{3,1}\theta^3\varepsilon + a_{2,2}\theta^2\varepsilon^2 + a_{1,3}\theta\varepsilon^3 + a_{0,4}\varepsilon^4. \end{aligned} \tag{9}$$

In the above expression symbol f represents the mechanical modulus (*i.e.* $f = E$, ν or μ), while symbol ε denotes the strain associated with it (*i.e.* $\varepsilon = \varepsilon_1$ for $f = E$ and $f = \nu$; while $\varepsilon = \varepsilon_6$ for $f = \mu$). The coefficients $a_{i,j}$ obtained from the nonlinear least squares fitting are listed in Table 2. We note that the calculated mean relative error (averaged over 42×201 or 42×101 – in the case of μ – points) was found

as 0.14%, 0.28% and 0.045% (for E, ν and μ, respectively), and the maximum relative error did not exceed 1.7%, 2.5% and 0.42%. This shows that the obtained fits accurately reproduce the 2D maps presented in Figure 5.

Table 2: Coefficients of polynomials (see Eq. (9)) describing nonlinear anisotropic mechanical behavior of penta-graphene. Here, angle θ is expressed in **degrees**. The unit for Young's modulus E and shear modulus μ is GPa nm.

Coefficient indices i, j	Young's modulus $E(\theta, \varepsilon_1)$	Poisson's ratio $\nu(\theta, \varepsilon_1)$	Shear modulus $\mu(\theta, \varepsilon_6)$
0, 0	2.425206×10^{2}	-8.251884×10^{-2}	1.624817×10^{2}
1, 0	7.541568×10^{-2}	-9.004087×10^{-4}	8.116323×10^{-2}
0, 1	-1.163927×10^{3}	-1.119765×10^{0}	-1.735933×10^{1}
2, 0	2.720296×10^{-2}	-3.284450×10^{-5}	-6.006031×10^{-2}
1, 1	-4.609653×10^{0}	1.508443×10^{-3}	-1.152805×10^{0}
0, 2	-1.234095×10^{3}	2.867903×10^{0}	-9.601932×10^{2}
3, 0	-3.496951×10^{-4}	-2.229375×10^{-6}	1.188480×10^{-3}
2, 1	-8.066811×10^{-2}	-3.209775×10^{-5}	8.676308×10^{-2}
1, 2	2.407700×10^{1}	6.118096×10^{-2}	-2.195936×10^{1}
0, 3	1.982593×10^{4}	-1.943642×10^{0}	-1.362941×10^{4}
4, 0	-1.138031×10^{-6}	5.146748×10^{-8}	-4.826035×10^{-6}
3, 1	2.261860×10^{-3}	1.165261×10^{-8}	-1.536743×10^{-3}
2, 2	-4.799477×10^{-1}	-1.295644×10^{-3}	8.399292×10^{-1}
1, 3	1.912602×10^{1}	-1.405455×10^{-1}	-3.761039×10^{0}
1, 4	-4.347723×10^{4}	1.215379×10^{1}	7.739685×10^{4}

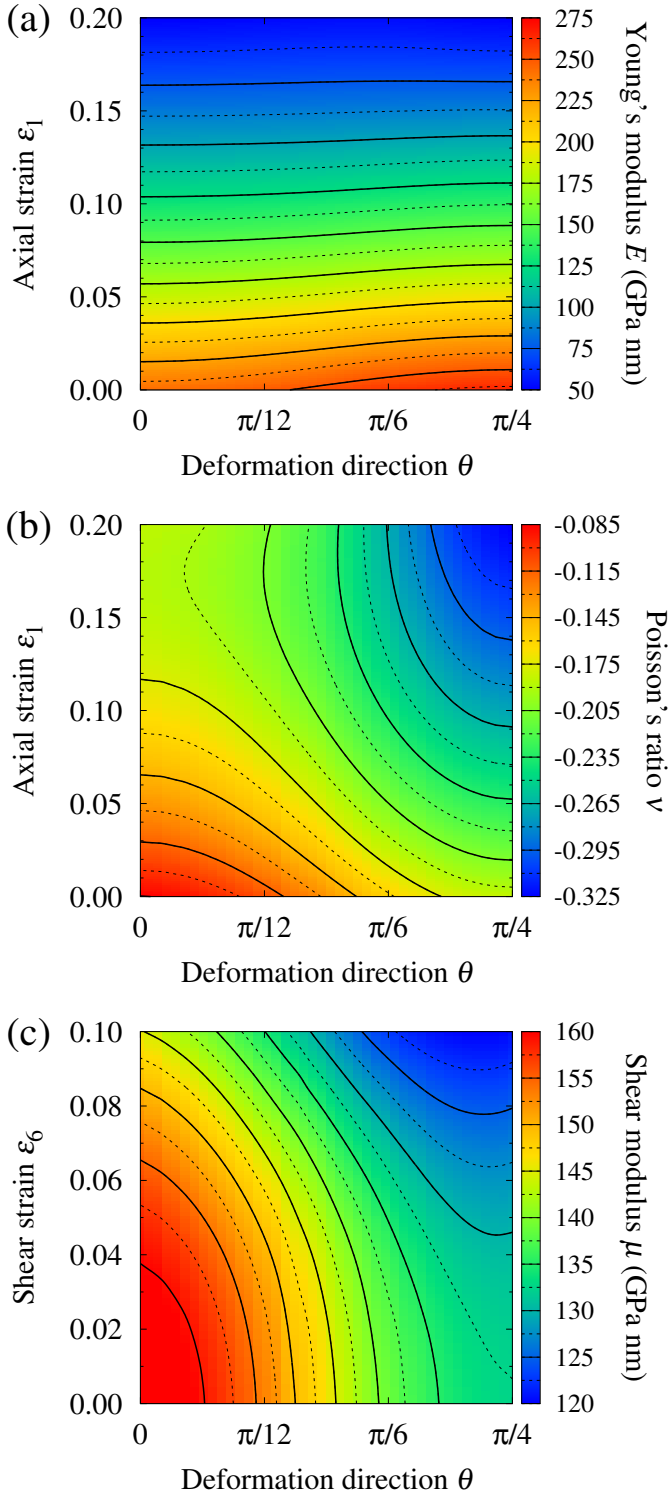

Figure 5: Contour plots showing the dependence of mechanical moduli of pentagraphene on deformation direction θ and strain: Young's modulus E (panel a), Poisson's ratio ν (panel b) and shear modulus μ (panel c).

4. Explanation of observed anisotropy

Now we will try to explain the observed anisotropy of the mechanical properties of PG. We will analyze in details two deformation directions, $\theta = 0$ and $\theta = \pi/4$, which – from the mechanical point of view – turned out to be significantly different and therefore can be considered as two main directions. First, we will introduce some concepts.

In fact, PG constitutes a lattice of carbon atoms connected with non-equivalent covalent bonds. The bonds which connect atoms C1 and C2 (we will denote them as 1-2 bonds) are less stiff than the bonds which connect two C2 atoms (2-2 bonds). The influence of these two types of bonds on the mechanical properties of PG is significantly different and changes when the deformation direction is changed.

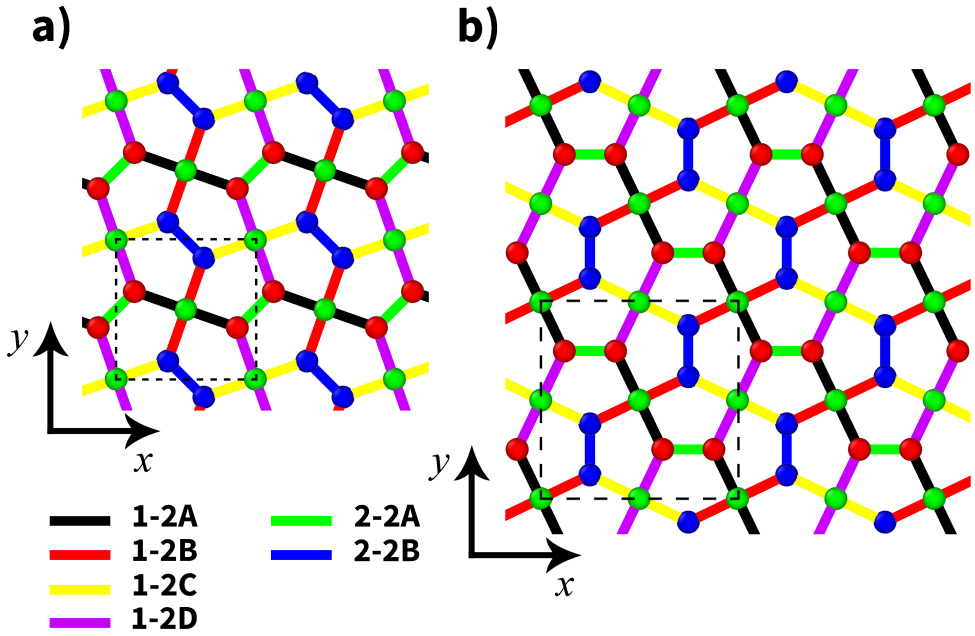

Figure 6: Six considered bond types. The PG structure is shown as it is oriented when deformation is carried out in direction $\theta = 0$ (panel a) and direction $\theta = \pi/4$ (panel b). On both panels the x axis is aligned with the axial direction, while the y axis corresponds to the transverse direction. Mechanically non-equivalent bonds (see text) are depicted with a different color. The six atom (panel a) and twelve atom (panel b) unit cells are shown.

To better illustrate this, in Figure 6 once again we show the structure of PG, presenting how it is oriented when the deformation is carried out in directions $\theta = 0$ (panel a) and $\theta = \pi/4$ (panel b). We distinguished (and depicted with a different color) six different bond types: 1-2A (black), 1-2B (red), 1-2C (yellow), 1-2D (violet), 2-2A (green) and 2-2B (blue). These types differ because of their i) different stiffness (1-2 vs 2-2) and ii) different role (compare 1-2A, ..., 1-2D bonds and 2-2A and 2-2B bonds). The latter is a consequence of a different orientation of specific bonds with respect to the deformation direction.

4.1. Young's modulus

First, we will focus on the anisotropy of Young's modulus E. When looking at the PG structure (Figure 6) in the context of uniaxial stretching significant differences are seen between the two considered deformation directions. The deformation carried out in direction $\theta = \pi/4$ strongly favors some of the 2-2 bonds. Half of them, namely the 2-2A bonds, are oriented parallel to the deformation direction, while their second half (*i.e.* 2-2B bonds) is perpendicular to it. As a result, during the stretching the 2-2A bonds are strongly stretched, while the 2-2B bonds are even shortened. This is clearly visible in Figure 7b which presents the dependencies of bond lengths on the strain. When moving from $\varepsilon_1 = 0$ to $\varepsilon_1 = 0.2$ the 2-2A bonds – which are much more "exposed" to the deformation – elongate by 6.3% of their initial length, while the 2-2B bonds shorten by 0.9%.

This situation changes when the deformation is carried out in direction $\theta = 0$. For this direction both types of the 2-2 bonds form an angle of $\pi/4$ with the direction of deformation and have the same influence on the course of deformation, as evidenced by the overlapping $d_{2-2\mathrm{A}}(\varepsilon_1)$ and $d_{2-2\mathrm{B}}(\varepsilon_1)$ characteristics (Figure 7a). For this direction the role played by the 2-2 bonds is somehow limited, as they do not elongate significantly, only by 1.6% of their initial length (compare with 6.3% elongation obtained for the 2-2A bonds and $\theta = \pi/4$).

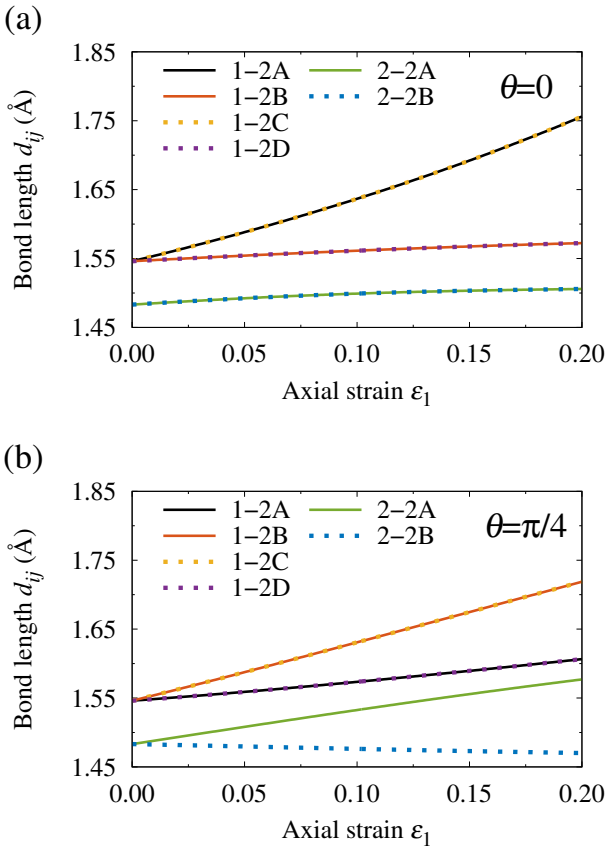

Figure 7: Changes of bond lengths in penta-graphene during uniaxial stretching. Two panels correspond to deformation carried out in directions $\theta = 0$ (panel a) and $\theta = \pi/4$ (panel b). Six characteristics correspond to six different bond types (see text).

The non-equivalence of roles is also visible in the case of the 1-2 bonds. For both the considered directions half of them (*i.e.* 1-2A and 1-2C bonds for $\theta = 0$, 1-2B and 1-2C bonds for $\theta = \pi/4$) form a smaller angle with the deformation direction and – as a result – are much more "exposed" to the deformation. The analysis of bond lengths (Figure 7) confirms that: when moving from $\varepsilon_1 = 0$ to $\varepsilon_1 = 0.2$ the indicated bonds elongate by as much as 13.6% ($\theta = 0$, 1-2A and 1-2C) and 11.2% ($\theta = \pi/4$, 1-2B and 1-2C) of their initial length. As opposed, the remaining 1-2 bonds, as they form a larger angle with the direction of deformation, are less "active" in the deformation process and – as a consequence – do not elongate significantly, by less than 2% (1-2B and 1-2D for $\theta = 0$) and 4% (1-2A and 1-2D for $\theta = \pi/4$).

The above analysis outlines important differences seen in the role played by individual bonds. However, as it is based on simple geometrical considerations only it does not allow qualifying these differences more accurately. This requires looking at the problem from an energetic perspective and can be done using decomposition of the potential energy defined by Equation (4). We used this decomposition to study how the energies V_{ij} of six considered bond types (1-2A, 1-2B, 1-2C, 1-2D, 2-2A and 2-2B) change during the deformation. The obtained $V_{ij}(\varepsilon_1)$ dependencies are presented in Figure 8.

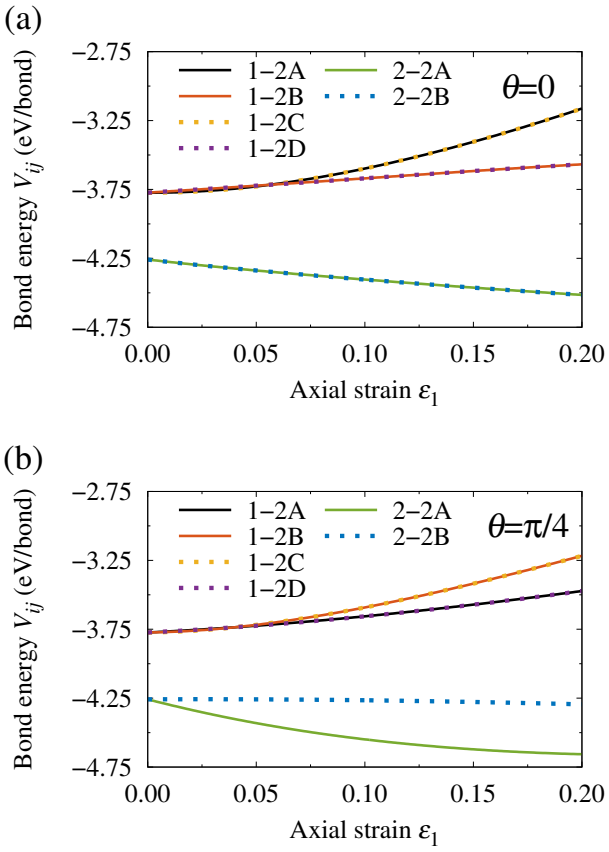

Figure 8: Changes of bond energies in penta-graphene during uniaxial stretching. Two panels correspond to deformation carried out in directions $\theta = 0$ (panel a) and $\theta = \pi/4$ (panel b). Six characteristics correspond to six different bond types (see text).

For the direction $\theta = 0$ the energy of all types of the 1-2 bonds increases, from -3.77 eV obtained for $\varepsilon_1 = 0$ to -3.16 eV (1-2A and 1-2C bonds) and -3.57 eV (1-2B and 1-2D bonds) obtained for $\varepsilon_1 = 0.2$. This comparison confirms the earlier finding that for $\theta = 0$ the 1-2A and 1-2C bonds are more "active" than the 1-2B and 1-2D bonds. An analysis of bond energies also confirms that in the deformation carried out for the second considered direction $\theta = \pi/4$ the 1-2B and 1-2C bonds are more "active", as their $V_{ij}(\varepsilon_1)$ characteristics lie above the characteristics corresponding to the 1-2A and 1-2D bonds. For this deformation direction the energy of all 1-2 bonds also increases with the increasing strain.

As opposed to the 1-2 bonds, the energy of both types of the 2-2 bonds decreases with the increasing strain. For $\theta = 0$ the characteristics obtained for the 2-2A and 2-2B bonds overlap, which confirms their identical role. For direction $\theta = \pi/4$ their role becomes diversified, as evidenced by significant differences seen between $V_{2-2\mathrm{A}}(\varepsilon_1)$ and $V_{2-2\mathrm{B}}(\varepsilon_1)$ characteristics. For this deformation direction, a strong change in the energy of the 2-2A bonds is visible (their energy changes by more than -0.4 eV when moving from $\varepsilon_1 = 0$ to $\varepsilon_1 = 0.2$), while the energy of the 2-2B bonds changes only slightly (by -0.04 eV).

An analysis of the bond energies V_{ij} also allows quantifying the influence of individual bond types on the total stiffness of PG (*i.e.* its Young modulus). For this purpose, we determined the dependency of the strain energy density for each considered bond type, defined as:

$$e_{ij}(\varepsilon_1) = \frac{N_{ij}\left[V_{ij}(\varepsilon_1) - V_{ij}(\varepsilon_1 = 0)\right]}{A_0}. \tag{10}$$

Here, A_0 denotes the area of the unit cell in the relaxed (unstrained) state, which is equal to $A_0 = a_0^2$ (for $\theta = 0$) and $A_0 = (\sqrt{2}a_0)^2 = 2a_0^2$ (for $\theta = \pi/4$). The a_0 symbol denotes the (equilibrium) lattice constant, which equals to $a_0 = 3.592$ Å. Symbol N_{ij} denotes the number of bonds of the ij-th type (ij = 1-2A, 1-2B, 1-2C, 1-2D, 2-2A or 2-2B) in the unit cell. We note that one six-atom unit cell of size $a_0 \times a_0$ (direction $\theta = 0$) has as many as eight "weaker" 1-2 bonds (two bonds for each of the four considered types: 1-2A, ..., 1-2D) and only two "stronger" 2-2 bonds (one of each type). The given numbers of bonds increase twice for the twelve-atom unit

cell of size $\sqrt{2}a_0 \times \sqrt{2}a_0$ (direction $\theta = \pi/4$).

The obtained $e_{ij}(\varepsilon_1)$ dependencies were fitted with the seventh degree polynomial. By examining their curvature, *i.e.* by calculating the second derivative:

$$E_{ij}(\varepsilon_1) = \frac{\partial^2 e_{ij}(\varepsilon_1)}{\partial \varepsilon_1^2}, \tag{11}$$

we determined the contributions $E_{ij}(\varepsilon_1)$ of the individual bonds to the strain dependent Young's modulus $E(\varepsilon_1)$. We will term the E_{ij} contribution as the effective stiffness of bonds of the ij-th type. Within such an approach, Young's modulus is given as a sum of the effective stiffnesses of the six considered bond types, *i.e.*:

$$E(\varepsilon_1) = E_{1-2\mathrm{A}}(\varepsilon_1) + E_{1-2\mathrm{B}}(\varepsilon_1) + E_{1-2\mathrm{C}}(\varepsilon_1) + E_{1-2\mathrm{D}}(\varepsilon_1) + E_{2-2\mathrm{A}}(\varepsilon_1) + E_{2-2\mathrm{B}}(\varepsilon_1). \tag{12}$$

The obtained $E_{ij}(\varepsilon_1)$ characteristics are presented in Figure 9.

Even the first glance shows that for $\theta = 0$ the total stiffness of PG is mainly determined by the very high stiffness of the 1-2A and 1-2C bonds. For $\varepsilon_1 = 0$ their effective stiffness was found as $E_{1-2\mathrm{A}} = E_{1-2\mathrm{C}} = 102$ GPa nm, which implies that they make up more than 85% of Young's modulus E. The contributions of other bonds were found as much smaller, not exceeding 13.8 GPa nm (the 2-2A and 2-2B bonds) and 4.9 GPa nm (the 1-2B and 1-2D bonds).

For the second considered direction $\theta = \pi/4$ the 1-2B and 1-2C bonds were found as giving the leading contributions (*ca.* 75% of E), with the effective stiffness (calculated for $\varepsilon_1 = 0$) being as high as $E_{1-2\mathrm{B}} = E_{1-2\mathrm{C}} = 98$ GPa nm, which is very similar to a value obtained for the 1-2A and 1-2C bonds and $\theta = 0$. What is interesting, it turned out that for $\theta = \pi/4$ the 2-2B bonds give a slightly negative (-4.4 GPa nm) contribution to E. The effective stiffnesses of the remaining bonds were found as $E_{2-2\mathrm{A}} = 30.9$ GPa nm and $E_{1-2\mathrm{A}} = E_{1-2\mathrm{D}} = 20.8$ GPa nm.

In order to summarize the obtained picture and see what the resultant role of the 1-2 and 2-2 bonds is (regardless of their orientation), it is useful to look at the total contributions

$$E_{1-2}(\varepsilon_1) = E_{1-2\mathrm{A}}(\varepsilon_1) + E_{1-2\mathrm{B}}(\varepsilon_1) + E_{1-2\mathrm{C}}(\varepsilon_1) + E_{1-2\mathrm{D}}(\varepsilon_1) \tag{13}$$

and

$$E_{2-2}(\varepsilon_1) = E_{2-2\mathrm{A}}(\varepsilon_1) + E_{2-2\mathrm{A}}(\varepsilon_1), \tag{14}$$

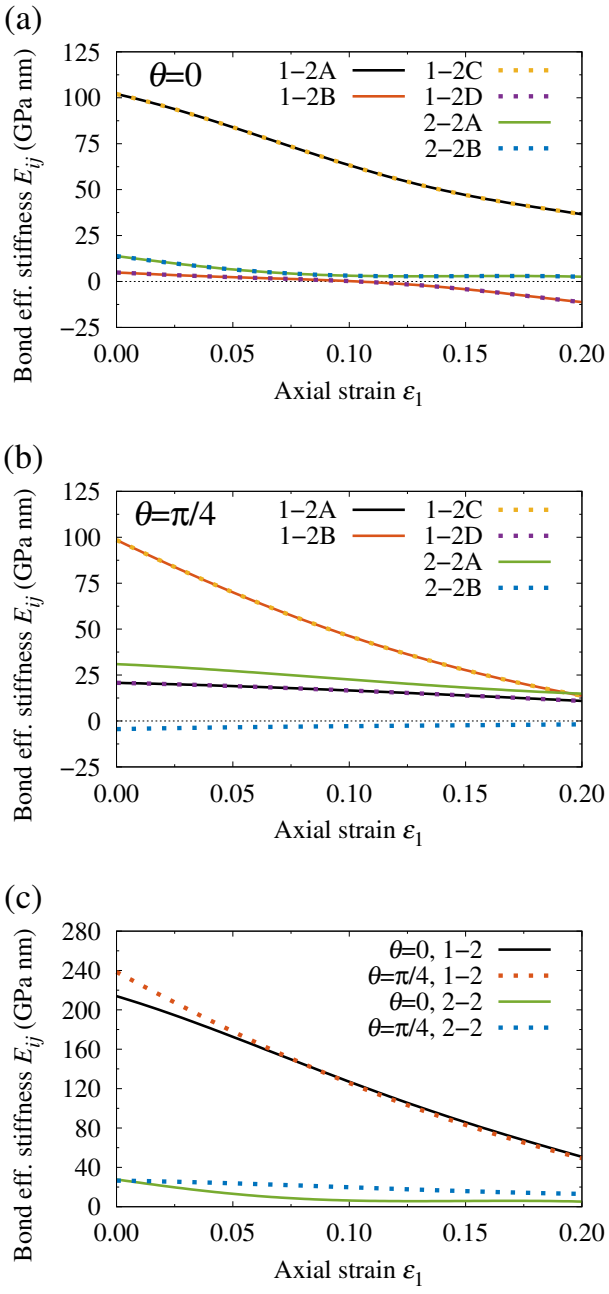

Figure 9: Effective stiffness of bonds in penta-graphene.

which are shown in Figure 9c. Such a look allows stating that at low deformations (*i.e.* close to $\varepsilon_1 = 0$) the anisotropy of Young's modulus is mostly a consequence of differences seen in the role played by the 1-2 bonds, and not a consequence of the characteristics of the 2-2 bonds. This is evidenced by the fact that at $\varepsilon_1 = 0$ the E_{1-2} contributions corresponding to $\theta = 0$ and $\theta = \pi/4$ turned out to be different (by almost 25 GPa nm), while the E_{2-2} contributions turned out to be almost

identical. This picture changes at high deformations. When moving from $\varepsilon_1 = 0$ to $\varepsilon_1 = 0.2$ the anisotropy of Young's modulus is to a decreasingly smaller degree a consequence of the characteristics of the 1-2 bonds, and to an increasing larger degree a consequence of the characteristics of the 2-2 bonds. This is evidenced by the fact that the E_{1-2} contributions corresponding to $\theta = 0$ and $\theta = \pi/4$ converge as the strain is increased (and above $\varepsilon_1 \approx 0.075$ become almost identical), while the E_{2-2} contributions continuously diverge.

In the above analysis we limited ourselves to two deformation directions only. However, a similar analysis performed for intermediate directions showed that the picture obtained for $\theta = 0$ smoothly transforms into the picture obtained for $\theta = \pi/4$, and no peculiarities are observed between these two main directions.

To complete this analysis we would like to point out that the presented approach is a kind of an effective look. In fact, when analyzing the bond energies V_{ij} we account for all effects that occur in the vicinity of the considered ij-th bond during the deformation, and not only for effects which are related to bond stretching. The many-body nature of V_{ij} causes that the effective stiffnesses E_{ij} also account for energy contributions which originate from changing the valence angles. As we limited ourselves to the presentation of bond length changes only, it must be noted here that the changes of valence angles also turned out to be significant. This can be well illustrated, for example, by the analysis of the angle β which measures the corrugation of PG (see Section 2.1). Our calculations showed that when the strain is increased from $\varepsilon_1 = 0$ to $\varepsilon_1 = 0.2$ this angle changes by as much as 19-25 degrees (for $\theta = \pi/4$ and $\theta = 0$, respectively), *i.e.* by 15%-20% of its initial value. This clearly shows that during the stretching of PG the process of angles deformation is very intense. We remind that the characteristics of the potential used in these studies (especially the nonlinear nature of the bond order term $\overline{b}_{ij}$, see discussion in Section 2.3) makes it impossible to assess quantitatively how the changing of specific valence angles affects Young's modulus (and other mechanical moduli) of PG.

4.2. Shear modulus

Now we will explain the anisotropy of the shear modulus μ, using the approach analogous to that applied in the case of Young's modulus E.

Even an intuitive look at the structure of PG (Figure 6) suggests that for $\theta = 0$ the shearing force (acting tangentially on the $+y$ edge in the $+x$ direction) should cause an elongation of the 1-2B, 1-2C and 2-2A bonds and shortening of the remaining 1-2A, 1-2D and 2-2B bonds. We observed this behavior in our simulations, as evidenced by the calculated dependencies of bond lengths on the shearing strain ε_6 (Figure 10a). A similar (*ca.* 2.4%-2.6%) increase in the bond length was observed for the first triple of bonds indicated above, while for the second triple similar (*ca.* 1.7%-1.9%) shortening was found.

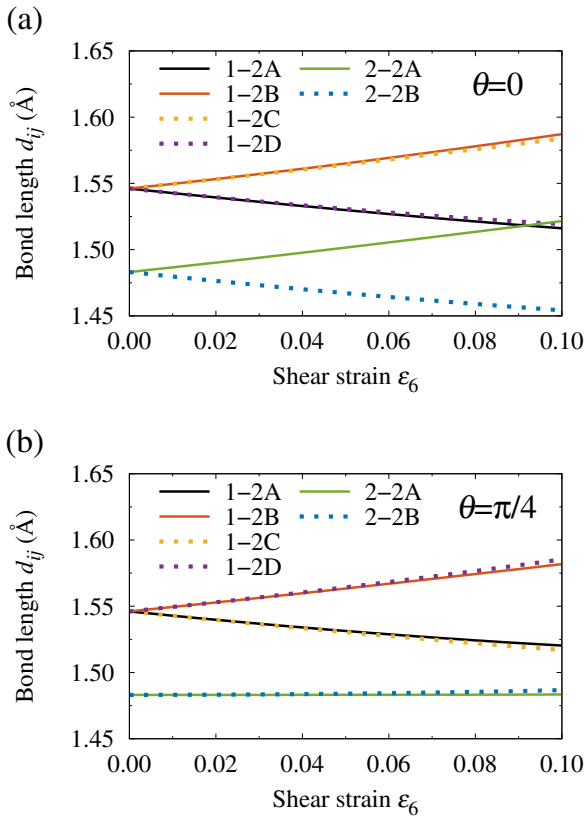

Figure 10: Changes in bond length in penta-graphene during simple shearing. The two panels correspond to deformation carried out in directions $\theta = 0$ (panel a) and $\theta = \pi/4$ (panel b). The six characteristics correspond to six different bond types (see text).

This picture changes significantly for $\theta = \pi/4$. Although the 1-2 bonds behave similarly (half of them – namely 1-2A and 1-2C – elongate and half of them – namely 1-2B and 1-2D – shorten, with similar elongations – *ca.* 2.3%-2.5% – and shortenings – *ca.* 1.7%-1.9%, see Figure 10b), for this deformation direction the 2-2 bonds behave completely differently, as their lengths almost do not change (the relative change in their length was found as 0.02% for 2-2A and 0.2% for 2-2B). This can be explained by a simple mechanical analog: since for $\theta = \pi/4$ the 2-2A/2-2B bonds become parallel/orthogonal to the direction of the shearing force they are not affected by it.

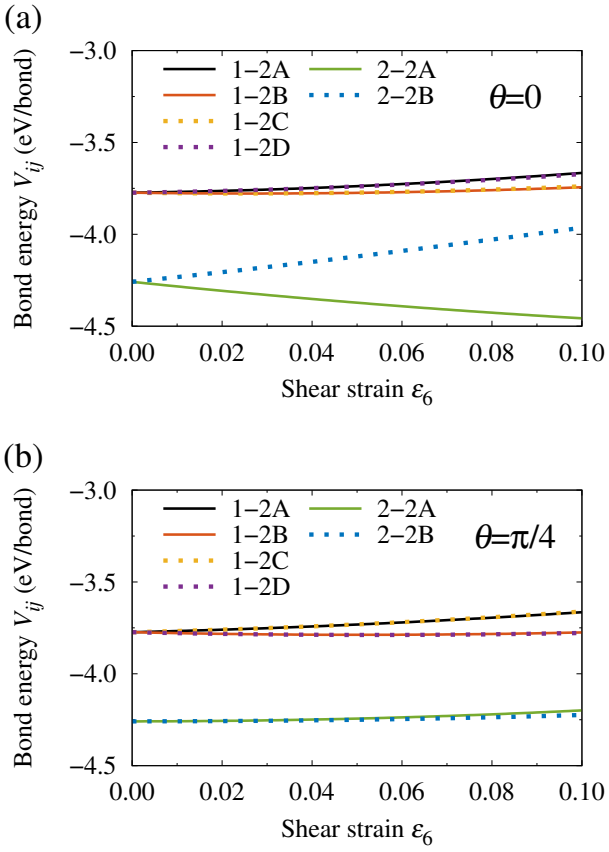

Figure 11: Changes of bond energies in penta-graphene during simple shearing. The two panels correspond to deformation carried out in directions $\theta = 0$ (panel a) and $\theta = \pi/4$ (panel b). The six characteristics correspond to six different bond types (see text).

This change in the role played by the 2-2 bonds is also revealed by the analysis of bond energies V_{ij} (Figure 11). For $\theta = 0$ the energy of both 2-2 bonds changes significantly, by approximately -0.2 eV (2-2A) and 0.3 eV (2-2B). For $\theta = \pi/4$ these changes turned out to be smaller by one order of magnitude (we obtained $V_{2-2\mathrm{A}}(\varepsilon_6 = 0.1) - V_{2-2\mathrm{A}}(\varepsilon_6 = 0) = 0.06$ eV and $V_{2-2\mathrm{B}}(\varepsilon_6 = 0.1) - V_{2-2\mathrm{B}}(\varepsilon_6 = 0) = 0.03$ eV).

Interesting results are provided by analysis of the contributions μ_{ij} of the individual bonds to the shear modulus μ. These contributions were determined in a way analogous to that used in the previous subsection, by calculating the following second derivative of the strain energy density:

$$\mu_{ij}(\varepsilon_6) = \frac{\partial^2 e_{ij}(\varepsilon_6)}{\partial \varepsilon_6^2}. \tag{15}$$

The contribution μ_{ij} will be termed as the effective rigidity of the bonds (of the ij-type).

The obtained dependencies $\mu_{ij}(\varepsilon_6)$ are presented in Figure 12. The 1-2 bonds give the highest contributions to the shear modulus, which are similar for all their types and for $\varepsilon_6 = 0$ equal to 33.5-35.1 GPa nm ($\theta = 0$) and 53.1-55.8 GPa nm ($\theta = \pi/4$). The contributions of the 2-2 bonds are much smaller, not exceeding 12.7 GPa nm ($\theta = 0$, $\varepsilon_6 = 0$) or 14.2 and 9.3 GPa nm ($\theta = \pi/4$, $\varepsilon_6 = 0$, 2-2A and 2-2B bonds, respectively).

The analysis of effective rigidities shows that the anisotropy of the shear modulus μ is mostly a consequence of the characteristics of all 1-2 bonds. For these bonds the effective rigidities μ_{ij} calculated for the direction $\theta = 0$ (Figure 12a) turned out to be significantly smaller than those calculated for the direction $\theta = \pi/4$ (Figure 12b). The total rigidity, captured by the sum:

$$\mu_{1-2} = \mu_{1-2A} + \mu_{1-2B} + \mu_{1-2C} + \mu_{1-2D}, \tag{16}$$

turned out to be lower for $\theta = 0$ by *ca.* 30 GPa nm than the value obtained for $\theta = \pi/4$ (see Figure 12c). On the other hand, the total contribution of the 2-2 bonds, *i.e.*:

$$\mu_{2-2} = \mu_{2-2A} + \mu_{2-2B}, \tag{17}$$

turned out to be almost identical. We found that at $\varepsilon_6 = 0$ it decreases only by *ca.* 2 GPa nm when the deformation direction is changed from $\theta = 0$ to $\theta = \pi/4$. This observation allows us to state that the 2-2 bonds do not contribute significantly to the observed anisotropy of the shear modulus μ, and it should be mainly attributed to the "weaker" 1-2 bonds.

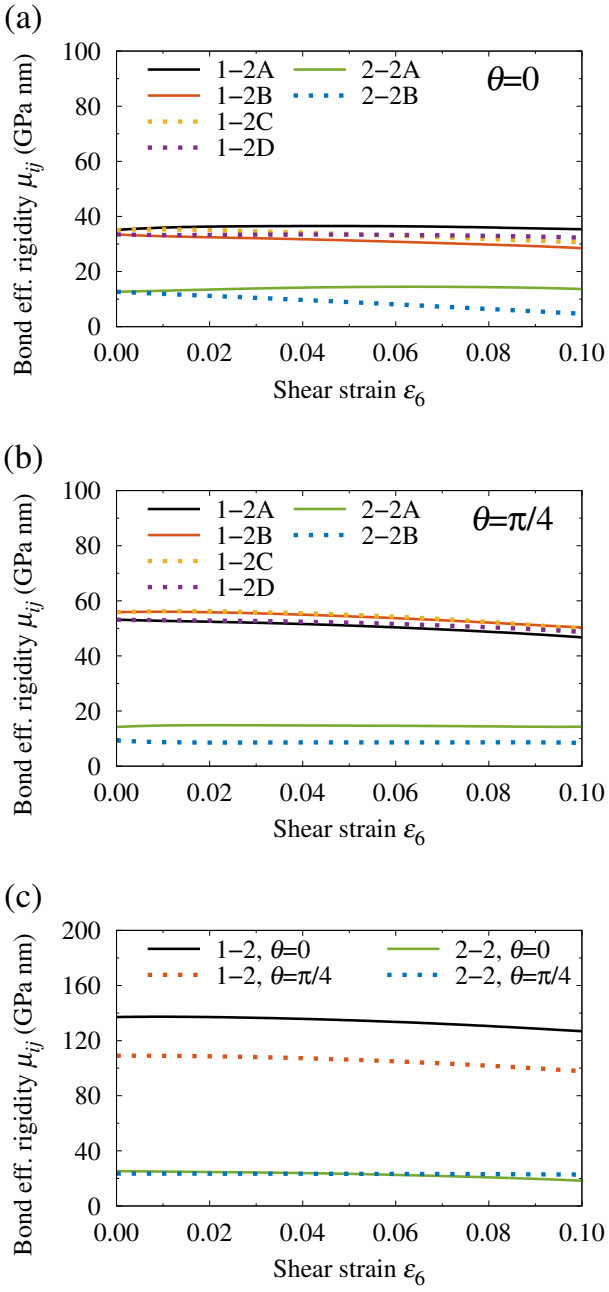

Figure 12: Effective rigidity of bonds in penta-graphene.

4.3. Poisson's ratio

The geometric nature of Poisson's ratio is the reason why an approach analogous to the one applied before, *i.e.* based on the decomposition of the strain energy into contributions coming from different bonds, can not be used in an attempt to explain its anisotropy. However, it is possible to decompose Poisson's ratio based on the geometric construction.

By using the lengths a and b of the unit cell sides its area A can be written as:

$$A(\varepsilon_1) = a(\varepsilon_1)b(\varepsilon_2) = \left[a_0(1+\varepsilon_1)\right]\left[b_0(1+\varepsilon_2(\varepsilon_1))\right]. \tag{18}$$

Here, symbols a_0 and b_0 denote the equilibrium lattice constants and the transverse strain ε_2 depends on the axial strain ε_1 through strain dependent Poisson's ratio (Eq. (6)).

By differentiating Eq. (18) with respect to ε_1 one obtains:

$$A'(\varepsilon_1) = a_0 b_0 \left[\big(1+\varepsilon_2(\varepsilon_1)\big) + \big(1+\varepsilon_1\big)\frac{\partial \varepsilon_2}{\partial \varepsilon_1}\right]. \tag{19}$$

Accounting for the fact that for PG $a_0 = b_0$ and by using Eq. (6) this can be written as:

$$\nu(\varepsilon_1) = -\frac{\partial \varepsilon_2}{\partial \varepsilon_1} = \frac{A(\varepsilon_1)}{a_0^2(1+\varepsilon_1)^2} - \frac{A'(\varepsilon_1)}{a_0^2(1+\varepsilon_1)}. \tag{20}$$

This expression relates strain dependent Poisson's ratio $\nu(\varepsilon_1)$ to the area of the unit cell A.

The usefulness of Eq. (20) originates from its linear nature (in terms of A), owing to which it is possible to decompose Poisson's ratio ν and write it as a sum of contributions coming from different building blocks forming the considered structure.

To illustrate this, in Figure 13 once again we have shown the structure of PG, this time distinguishing two building blocks, which form its lattice. The first block is made up of one C1 atom linked by 1-2 bonds with four C2 atoms. This block has a tetrahedral shape, therefore we will denote it with the TET symbol. The second block is constituted by a pair of C2 atoms linked by a 2-2 bond. It is spanned by four TET blocks and has the shape of a bent parallelogram, therefore we will

denote it with the PAR symbol. It is worth noting that one unit cell of PG has two TET blocks and two PAR blocks. Moreover, for each block type two subtypes can be distinguished, which have different orientation with respect to the deformation direction. We will denote these subtypes as TET-A, TET-B, PAR-A and PAR-B. They are also marked in Figure 13.

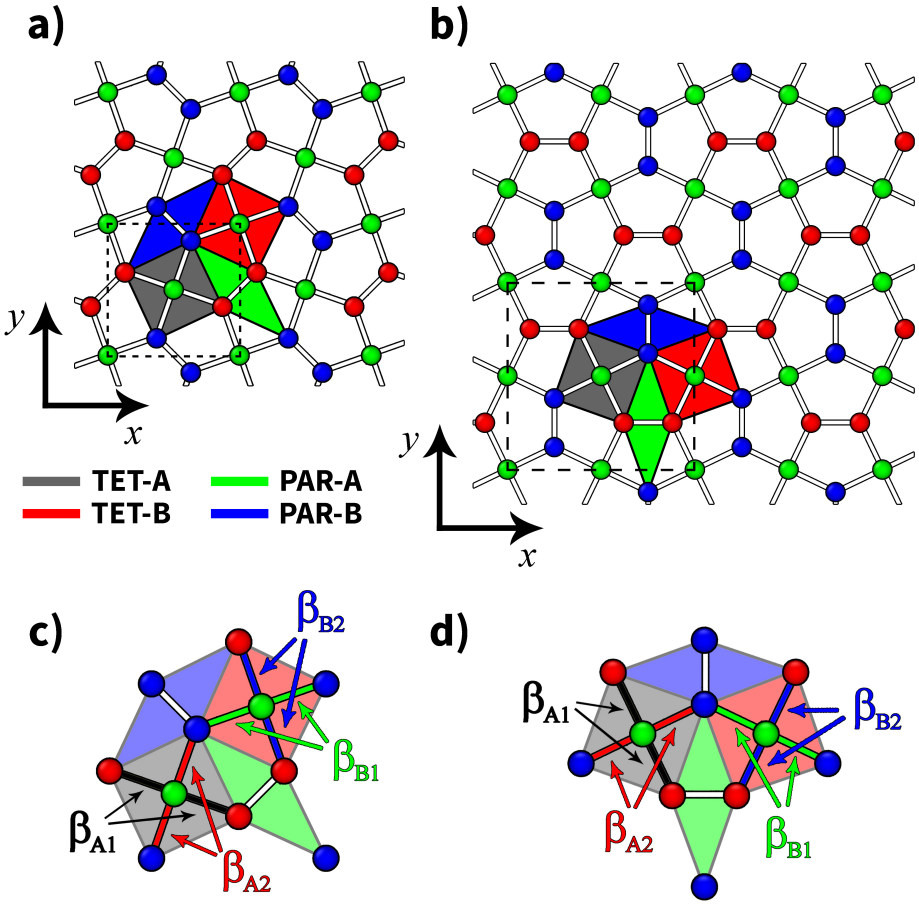

Figure 13: Structural building blocks in penta-graphene. The PG structure is shown as it is oriented when the deformation is carried out in direction $\theta = 0$ (panels a and c) and direction $\theta = \pi/4$ (panels b and d). Panels a and b present the four considered building blocks (TET-A, TET-B, PAR-A and PAR-B, see text), which are depicted by filled areas. On panels c and d we show four considered valence angles (β_{A1}, β_{A2}, β_{B1} and β_{B2}, see text), which measure the corrugation of PG. Each angle was depicted by coloring two bonds that make it. All angles lie in planes which are perpendicular to the plane of picture.

The PG unit cell area can be written as:

$$A = A_{\text{TET-A}} + A_{\text{TET-B}} + A_{\text{PAR-A}} + A_{\text{PAR-B}}, \tag{21}$$

i.e. as a sum of the areas of orthogonal projections of blocks on the $z = 0$ plane. This allows us to write Poisson's ratio of PG as a sum of four contributions:

$$\nu = \nu_{\text{TET-A}} + \nu_{\text{TET-B}} + \nu_{\text{PAR-A}} + \nu_{\text{PAR-B}}, \tag{22}$$

where the contribution ν_{BLO} (here, BLO = TET-A, TET-B, PAR-A or PAR-B) is given as:

$$\nu_{\text{BLO}}(\varepsilon_1) = \frac{A_{\text{BLO}}(\varepsilon_1)}{a_0^2(1+\varepsilon_1)^2} - \frac{A'_{\text{BLO}}(\varepsilon_1)}{a_0^2(1+\varepsilon_1)}. \tag{23}$$

Based on these expressions it is possible to determine Poisson's ratio for each of the considered blocks. This allows us to identify blocks which are responsible for i) the negativity and ii) the anisotropy of ν.

Using the approach introduced above, we analyzed the results corresponding to the uniaxial stretching. At the beginning, we examined how the A_{BLO} areas changed during the deformation. The obtained $A_{\text{BLO}}(\varepsilon_1)$ dependencies were fitted with fourth degree polynomials. Then, by differentiating them and by using Eq. (23), we calculated the contributions $\nu_{\text{BLO}}(\varepsilon_1)$. The obtained results are presented in Figure 14.

In the case of deformation carried out in direction $\theta = 0$ (Figure 14a) both TET blocks behave in an identical way, which is evidenced by the overlapping of their $\nu_{\text{BLO}}(\varepsilon_1)$ characteristics. The situation is similar in the case of the PAR blocks, both of which also play an identical role. A comparison of TET and PAR blocks shows their different role. The former give negative contributions to Poisson's ratio (we obtained $\nu_{\text{TET-A}}(\varepsilon_1 = 0) = \nu_{\text{TET-B}}(\varepsilon_1 = 0) = -0.074$ and $\nu_{\text{TET-A}}(\varepsilon_1 = 0.2) = \nu_{\text{TET-B}}(\varepsilon_1 = 0.2) = -0.113$), while the latter increase its value (we obtained $\nu_{\text{PAR-A}}(\varepsilon_1 = 0) = \nu_{\text{PAR-B}}(\varepsilon_1 = 0) = 0.032$ and $\nu_{\text{PAR-A}}(\varepsilon_1 = 0.2) = \nu_{\text{PAR-B}}(\varepsilon_1 = 0.2) = 0.019$).

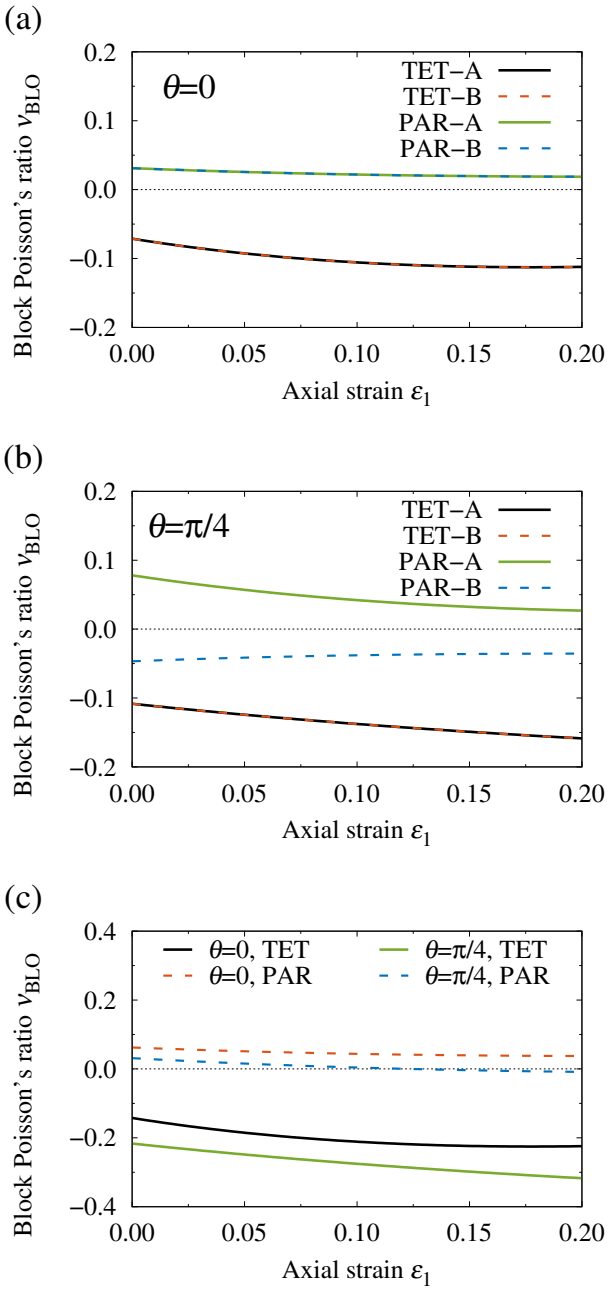

Figure 14: Poisson's ratio of different building blocks.

When moving to direction $\theta = \pi/4$ (Figure 14b) the qualitative role of the TET blocks does not change and they still give negative contributions to Poisson's ratio (we obtained $\nu_{\text{TET-A}}(\varepsilon_1 = 0) = \nu_{\text{TET-B}}(\varepsilon_1 = 0) = -0.108$ and $\nu_{\text{TET-A}}(\varepsilon_1 = 0.2) = \nu_{\text{TET-B}}(\varepsilon_1 = 0.2) = -0.159$), However, for this deformation direction the role of the PAR blocks is diversified. Half of them, namely the PAR-A blocks, still increase the value of ν (we obtained $\nu_{\text{PAR-A}}(\varepsilon_1 = 0) = 0.078$ and $\nu_{\text{PAR-A}}(\varepsilon_1 = 0.2) = 0.027$), but

their second half decrease it (we obtained $\nu_{\text{PAR-B}}(\varepsilon_1 = 0) = -0.047$ and $\nu_{\text{PAR-B}}(\varepsilon_1 = 0.2) = -0.035$).

The above analysis shows that the auxeticity of PG should be mainly attributed to the presence of the TET blocks. It also allows explaining the anisotropy of ν. In Figure 14c we present the total characteristics

$$\nu_{\text{TET}} = \nu_{\text{TET-A}} + \nu_{\text{TET-B}} \tag{24}$$

and

$$\nu_{\text{PAR}} = \nu_{\text{PAR-A}} + \nu_{\text{PAR-B}}. \tag{25}$$

Having analyzed them it becomes clear that the observed anisotropy cannot be attributed to a single block type (TET or PAR), because the change of θ from 0 to $\pi/4$ results in comparable changes in ν_{TET} and ν_{PAR} contributions (ν_{TET} and ν_{PAR} decrease by about 0.07-0.09 and 0.03-0.05, respectively).

The above analysis shows that the negativity of Poisson's ratio is mainly a consequence of the behavior of the TET blocks. However, the auxeticity of PG cannot be only explained by the presence of the TET blocks. In fact, it is a consequence of the specificity of both types of blocks. The role of the PAR blocks is equally important: by connecting the TET blocks with stiff 2-2 bonds, they are the reason why the deformation of PG goes mainly through the flattening of easily deformable tetrahedrons.

The picture of PG deformation obtained in this work is in accordance with the results of Sun *et al.* [11], who based on the DFT calculations concluded that the auxeticity of PG results from (as they called it) de-wrinkling mechanism. To show how significant this effect is, in Figure 15a we show how the thickness of PG (defined as $2h$, see Section 2.1) changes during uniaxial stretching. It is clearly visible that the flattening effect is i) very strong and ii) stronger for the deformation carried out in direction $\theta = \pi/4$ (when the strain is increased from $\varepsilon_1 = 0$ to $\varepsilon_1 = 0.2$ the thickness $2h$ decreases by 23% and 28% for $\theta = 0$ and $\theta = \pi/4$, respectively). The second observation explains the more negative values of Poisson's ratio obtained for $\theta = \pi/4$.

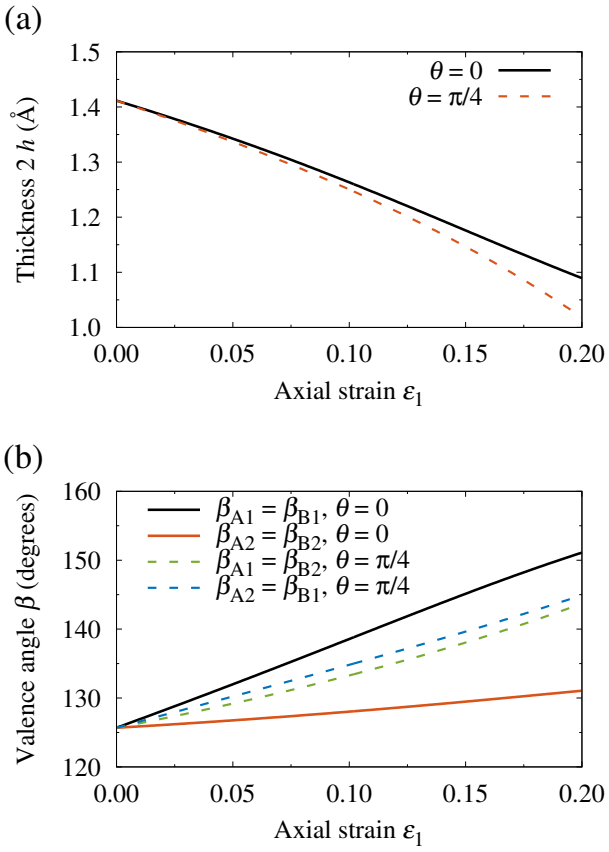

Figure 15: Changes in thickness (panel a) and corrugation (panel b) of pentagraphene during uniaxial stretching.

The described flattening effect can be also analyzed with the use of the β angle (see Section 2.1), which measures the corrugation of PG. In fact, four such angles can be defined (they are depicted in Figure 13), two for each considered TET block. For $\theta = 0$ the angles β_{A1} and β_{B1} mainly measure the structure flattening in the axial (x) direction, while the angles β_{A2} and β_{B2} describe this flattening along the transverse (y) direction. For $\theta = \pi/4$ this situation changes: β_{A2} and β_{B1} correspond to the axial direction, while the β_{A1} and β_{B2} angles correspond to the transverse direction. We note that an increase in the value of β angle indicates that the flattening along the corresponding direction takes place (an angle equal to 180 degrees corresponds to a completely flat structure).

The obtained $\beta(\varepsilon_1)$ dependencies are presented in Figure 15b. The most pronounced flattening is observed for $\theta = 0$ along the x direction ($\beta_{A1}(\varepsilon_1) = \beta_{B1}(\varepsilon_1)$

increase the fastest). However, for $\theta = 0$ the flattening along the transverse direction turned out to be smaller than for $\theta = \pi/4$ (compare $\beta_{\mathrm{A2}}(\varepsilon_1) = \beta_{\mathrm{B2}}(\varepsilon_1)$ obtained for $\theta = 0$ with $\beta_{\mathrm{A1}}(\varepsilon_1) = \beta_{\mathrm{B2}}(\varepsilon_1)$ obtained for $\theta = \pi/4$). This means that for $\theta = 0$ the expansion of PG structure along the transverse direction is less intense than for $\theta = \pi/4$. This observation explains once again the more negative values of ν obtained for $\theta = \pi/4$. It also shows how important – for the mechanics of PG – the angular deformation is.

In this place we would like to refer to work [32], in which we investigated the influence of double vacancies of the 5-8-5 type on the mechanical properties of graphene. We showed there that after introducing a large amount of these defects (*ca.* 0.5%–3%) the graphene sheet becomes wrinkled. During the stretching of such a structure the introduced wrinkles are flattened. This process leads to an increase in the area of the structure in the plane of deformation and results in auxetic behavior. The mechanism of PG auxeticity is therefore similar to the mechanism found for the defective graphene, as it also resembles the flattening of the initially corrugated structure.

In the description of this type of auxeticity – resulting from the wrinkage of the structure – the criterion given by Eq. (23) plays a particularly important role. By requiring that $\nu_{\mathrm{BLO}} < 0$ this criterion can be written as:

$$A'_{\mathrm{BLO}}(\varepsilon_1) > \frac{A_{\mathrm{BLO}}(\varepsilon_1)}{1 + \varepsilon_1}. \tag{26}$$

The above expression informs, how the projected area A_{BLO} should behave during the deformation. If the above inequality is satisfied, then the considered building block contributes to the auxetic behavior, giving negative contribution to the Poisson's ratio of the entire structure. Since this condition links the microscopic feature (variation of area A_{BLO}) with the macroscopic consequence (Poisson's ratio negativity), we believe that it will be very useful in studies on 2D auxeticity based on the crumpled paper mechanism.

5. Mechanical properties at finite temperature

5.1. Simulation protocol

We carried out a series of MD simulations to investigate the influence of temperature T on the mechanical moduli (E, ν and μ) of penta-graphene. Here, we limited our studies to four representative deformation directions ($\theta = 0, \pi/12, \pi/6$ and $\pi/4$) and considered the temperatures between 50 and 600 K, with the 50 K temperature interval. The calculations corresponding to one set of conditions (T, θ) consisted of two series of simulations, in which we studied the behavior of PG during i) uniaxial stretching ($\sigma_1 \neq 0, \sigma_2 = \sigma_6 = 0$) and ii) simple shearing ($\sigma_1 = \sigma_2 = 0, \sigma_6 \neq 0$). In the case of simulations corresponding to finite temperature we had to restrict the range of the studied stresses. This is motivated by the fact that at finite temperatures the PG structure breaks at stresses lower than at 0 K. For the uniaxial stretching we considered 31 different stresses σ_1, from the range $[0, 15]$ GPa nm, while for the simple shearing we considered 21 different stresses σ_6, from the range $[-0.4, 0.4]$ GPa nm.

All the MD simulations were performed in the isobaric-isothermal ensemble NpT. Pressure p and temperature T were controlled with a Parrinello-Rahman barostat [33] and a Nosé-Hoover thermostat [34, 35], both as implemented [36–38] in the LAMMPS program [30, 39, 40], which we used to perform the calculations. The equations of motion were integrated with the velocity Verlet algorithm [41], with the timestep length taken as $\Delta t = 0.5$ fs. The sizes of the simulated systems and the periodic boundary conditions were chosen identically as in the case of the MS simulations.

The simulation corresponding to a single stress state $(\sigma_1, \sigma_2, \sigma_6)$ consisted of 25 000 steps of the (initial) equilibration followed by 100 000 steps of sampling during which the information about the system was collected. This simulation was repeated 15 times, each time starting with a different initial condition, varied by changing the seed used for the random generation of the initial velocities. This allowed us to assess the uncertainty of the obtained results. To show the scale of the performed calculations we note that the entire series of simulations (12 temperatures, 4 deformation directions, 15 seeds, 31 and 21 stresses) consisted of about

4.7×10^9 MD steps.

After performing simulations for all the studied cases we calculated the corresponding system sizes L_x, L_y, X_y and the actual values of stresses σ_1, σ_2 and σ_6 by using time averaging. This allowed us to construct the $\sigma_1(\varepsilon_1)$, $\varepsilon_2(\varepsilon_1)$ and $\sigma_6(\varepsilon_6)$ characteristics, which we used to find the moduli E, ν and μ. We calculated them using an approach analogous to that used in the case of MS calculations, *i.e.* by fitting the obtained strain-stress (or strain-strain) dependencies with polynomials and then differentiating them. The obtained moduli were averaged over the performed runs, which allowed us to assess their uncertainties.

5.2. Results

In Figure 16 (panels a-c) we show how the strain dependent mechanical moduli of PG vary with the temperature, presenting the results obtained for three temperatures (0, 300 and 600 K) and two deformation directions ($\theta = 0$ and $\pi/4$). As it is clearly visible the temperature does not affect significantly the $E(\varepsilon_1)$ and $\mu(\varepsilon_6)$ characteristics, shifting them slightly towards lower values. In the case of Poisson's ratio a shift towards less negative values is observed, especially at lower ε_1 strains.

In order to quantify the influence of temperature more accurately, in Figure 16 (panels d-f) we present how the zero strain moduli depend on the temperature T. When the temperature is increased from 0 to 600 K the Young's modulus and the shear modulus decrease, by approximately 4–5% (E) and 6–9% (μ) of their initial (*i.e.* 0 K) value. In contrast to this, the Poisson's ratio increases with the temperature, but changes only by 8-14% of its 0 K value and remains negative even at the highest considered temperature. This holds for all studied deformation directions and shows that PG displays complete auxetic behavior in a wide range of temperatures.

All the three moduli depend almost linearly on temperature T in the considered temperature range. This holds for all the four considered deformation directions and it is evidenced by the fact that the linear interpolants (represented in Figure 16 by dashed lines) of the form $f(T) = f_0 + f_T T$ (here, $f = E, \nu$ or μ) are good fits to the data. In Table 3 we present the parameters of the obtained fits to facilitate

the use of our results (*e.g.* in continuum modeling of PG). We note that when performing the fitting, the modulus f_0 (corresponding to $T = 0$ K) was taken as the result of MS calculations and we optimized only coefficient f_T, which describes the temperature dependence of modulus f.

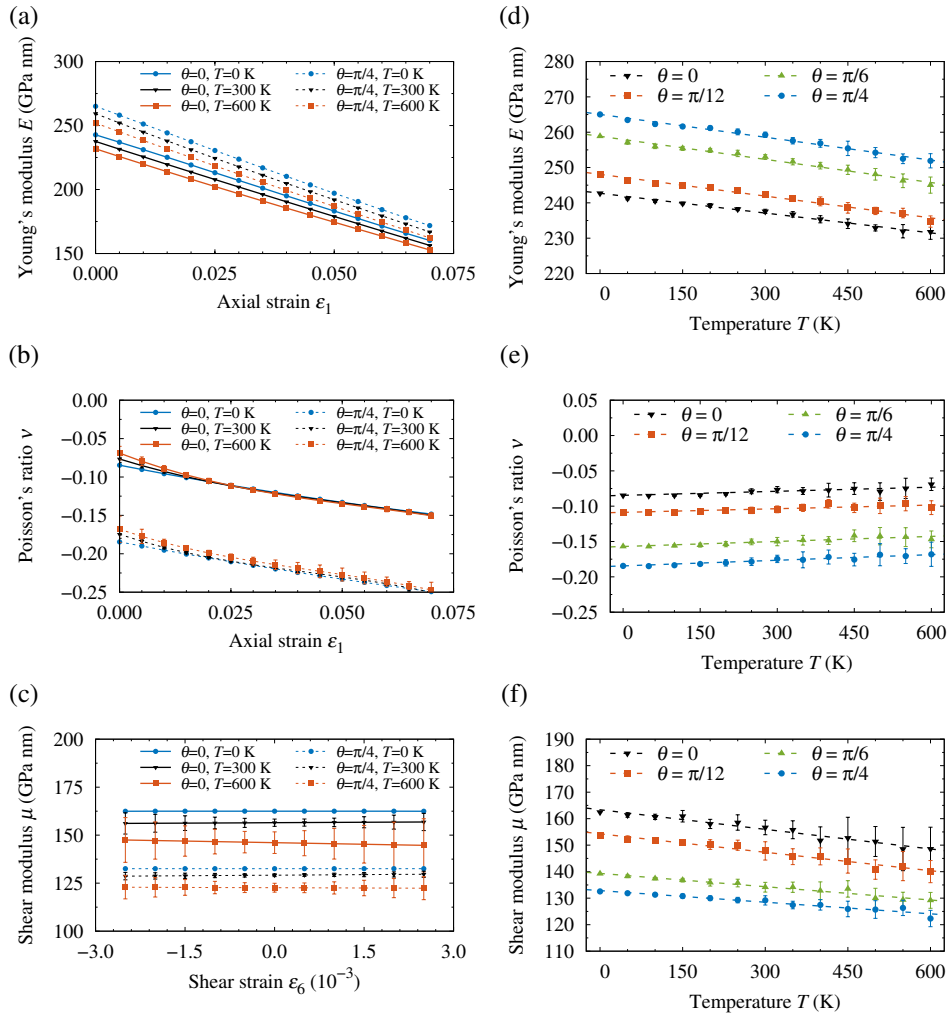

Figure 16: Influence of temperature on mechanical properties of PG: strain dependent mechanical moduli (panels a-c) and temperature dependence of zero strain mechanical moduli (panels d-e). The 0 K results were taken from the MS simulations. For $T > 0$ K the points and error bars represent mean and standard deviation of the results obtained from 15 independent simulations.

Table 3: Temperature dependence of zero strain mechanical moduli. Linear fit coefficients are presented (see text). The unit for E_0 and μ_0 is GPa nm, while the unit for E_T and μ_T is MPa nm K^{-1}. The unit for ν_T is 10^{-6} K^{-1}.

Direction	Young's modulus		Poisson's ratio		Shear modulus	
θ (rad)	E_0	E_T	ν_0	ν_T	μ_0	μ_T
0	242.7	−18.67	−0.0847	19.22	162.5	−24.65
$\pi/12$	248.1	−20.52	−0.1087	17.21	153.7	−23.20
$\pi/6$	258.8	−21.78	−0.1570	23.78	139.2	−16.73
$\pi/4$	265.0	−21.55	−0.1845	26.57	132.5	−14.59

6. Summary

In this work we investigated the mechanical properties of penta-graphene, a recently proposed carbon allotrope. We calculated three in-plane elastic moduli of PG and characterized their dependence on the deformation direction, strain and temperature using molecular statics and molecular dynamics simulations combined with the empirical description of the interatomic interactions.

Our results showed that Young's modulus E did not depend strongly on the deformation direction, as opposed to Poisson's ratio ν and the shear modulus μ, which we found as strongly anisotropic. According to our model the zero strain moduli vary between 243 and 265 GPa nm (E), −0.185 and −0.085 (ν), and 132 and 162 GPa nm (μ). These extreme values correspond to $\langle 100 \rangle$ (maximum of ν, minimum of E and μ) and $\langle 110 \rangle$ (minimum of ν, maximum of E and μ) crystallographic directions.

We found that all three E, ν and μ moduli decreased with an increase in the corresponding strain. The shear modulus μ turned out not to depend strongly on the strain, as opposed to E and ν, for which we observed a strong dependence, leading to a 2-fold (observed for ν) or even 5-fold (found for E) decrease in the modulus value, when the strain was increased from 0 to 0.2.

We studied how different (non-equivalent from the chemical point of view) carbon-carbon bonds contributed to the mechanical response of PG by analyzing bond energies. We showed that bonds which form diamond-like tetrahedral units

(and connect sp^2- and sp^3-hybridizied atoms in the structure of PG) gave the highest contribution to Young's modulus of PG, being responsible for almost 90% of its total stiffness. The shear modulus was also found to be dominated by these contributions, which make (again) about 90% of the total rigidity of PG. The analysis of energetics also showed that the anisotropy of Young's modulus was a consequence of the characteristics of both types of bonds present in PG. As opposed to that, we found that the anisotropy of the shear modulus should be mostly attributed to diamond-like bonds.

We analyzed the auxeticity of PG in detail and showed that PG had negative Poisson's ratio for all deformation directions and therefore should be considered as a completely auxetic structure. By studying the geometry changes which accompany deformation we demonstrated that the auxeticity of PG was mainly a consequence of the characteristics of the diamond-like tetrahedral units. We showed that the mechanism of PG auxeticity was similar to that of defective graphene, as it also resembled the behavior of crumpled paper. In an attempt to generalize our analysis we formulated a criterion for a two-dimensional auxeticity originating from this – so-called de-wrinkling – mechanism. This criterion allows determining which structural blocks contribute to auxeticity and to what extent.

We also investigated the influence of temperature showing that it only slightly affected the mechanical moduli of PG. For all the three considered mechanical moduli (E, μ, ν) we found that their dependence on the temperature could be well described with a linear function. Our simulations showed that both Young's modulus E and the shear modulus μ decreased with temperature. For Poisson's ratio we have found that it increases towards less negative values when the temperature is increased but – even at high temperatures – it remains negative. This shows that PG displays complete auxeticy in a wide range of temperatures.

Acknowledgements

We acknowledge the support of the TASK Academic Computer Centre (Gdańsk, Poland). This research was also supported in part by the PL-Grid Infrastructure (Grant POIG.02.03.00-00-096/10).

References

[1] S. Zhang, J. Zhou, Q. Wang, X. Chen, Y. Kawazoe, P. Jena, Penta-graphene: A new carbon allotrope, Proceedings of the National Academy of Sciences 112 (8) (2015) 2372–2377. arXiv:http://www.pnas.org/content/112/8/2372.full.pdf, doi:10.1073/pnas.1416591112.
URL http://www.pnas.org/content/112/8/2372.abstract

[2] P. Avramov, V. Demin, M. Luo, C. H. Choi, P. B. Sorokin, B. Yakobson, et al., Translation symmetry breakdown in low-dimensional lattices of pentagonal rings, The Journal of Physical Chemistry Letters 6 (22) (2015) 4525–4531, pMID: 26582476. arXiv:http://dx.doi.org/10.1021/acs.jpclett.5b02309, doi:10.1021/acs.jpclett.5b02309.
URL http://dx.doi.org/10.1021/acs.jpclett.5b02309

[3] C. P. Ewels, X. Rocquefelte, H. W. Kroto, M. J. Rayson, P. R. Briddon, M. I. Heggie, Predicting experimentally stable allotropes: Instability of penta-graphene, Proceedings of the National Academy of Sciences 112 (51) (2015) 15609–15612. arXiv:http://www.pnas.org/content/112/51/15609.full.pdf, doi:10.1073/pnas.1520402112.
URL http://www.pnas.org/content/112/51/15609.abstract

[4] W. Xu, G. Zhang, B. Li, Thermal conductivity of penta-graphene from molecular dynamics study, The Journal of Chemical Physics 143 (15) (2015) 154703. doi:http://dx.doi.org/10.1063/1.4933311.
URL http://scitation.aip.org/content/aip/journal/jcp/143/15/10.1063/1.4933311

[5] Z. G. Yu, Y.-W. Zhang, A comparative density functional study on electrical properties of layered penta-graphene, Journal of Applied Physics 118 (16) (2015) 165706. arXiv:http://dx.doi.org/10.1063/1.4934855, doi:10.1063/1.4934855.
URL http://dx.doi.org/10.1063/1.4934855

[6] G. R. Berdiyorov, G. Dixit, M. E. Madjet, Band gap engineering in penta-graphene by substitutional doping: first-principles calculations, Journal of Physics: Condensed Matter 28 (47) (2016) 475001.
URL http://stacks.iop.org/0953-8984/28/i=47/a=475001

[7] S. W. Cranford, When is 6 less than 5? penta- to hexa-graphene transition, Carbon 96 (2016) 421 – 428. doi:http://dx.doi.org/10.1016/j.carbon.2015.09.092.
URL http://www.sciencedirect.com/science/article/pii/S0008622315303109

[8] X. Li, S. Zhang, F. Q. Wang, Y. Guo, J. Liu, Q. Wang, Tuning the electronic and mechanical properties of penta-graphene via hydrogenation and fluorination, Phys. Chem. Chem. Phys. 18 (2016) 14191–14197. doi:10.1039/C6CP01092J.
URL http://dx.doi.org/10.1039/C6CP01092J

[9] B. Rajbanshi, S. Sarkar, B. Mandal, P. Sarkar, Energetic and electronic structure of penta-graphene nanoribbons, Carbon 100 (2016) 118 – 125. doi:http://dx.doi.org/10.1016/j.carbon.2016.01.014.
URL http://www.sciencedirect.com/science/article/pii/S0008622316300148

[10] T. Stauber, J. I. Beltrán, J. Schliemann, Tight-binding approach to penta-graphene, Scientific Reports 6 (2016) 22672. doi:10.1038/srep22672.
URL http://dx.doi.org/10.1038/srep22672

[11] H. Sun, S. Mukherjee, C. V. Singh, Mechanical properties of monolayer penta-graphene and phagraphene: a first-principles study, Phys. Chem. Chem. Phys. 18 (2016) 26736–26742. doi:10.1039/C6CP04595B.
URL http://dx.doi.org/10.1039/C6CP04595B

[12] Z. Wang, F. Dong, B. Shen, R. Zhang, Y. Zheng, L. Chen, S. Wang, C. Wang, K. Ho, Y.-J. Fan, B.-Y. Jin, W.-S. Su, Electronic and optical properties of novel carbon allotropes, Carbon 101 (2016) 77 – 85.

doi:https://doi.org/10.1016/j.carbon.2016.01.078.
URL http://www.sciencedirect.com/science/article/pii/S0008622316300665

[13] F. Q. Wang, J. Yu, Q. Wang, Y. Kawazoe, P. Jena, Lattice thermal conductivity of penta-graphene, Carbon 105 (2016) 424 – 429. doi:https://doi.org/10.1016/j.carbon.2016.04.054.
URL http://www.sciencedirect.com/science/article/pii/S0008622316303256

[14] X. Wu, V. Varshney, J. Lee, T. Zhang, J. L. Wohlwend, A. K. Roy, et al., Hydrogenation of penta-graphene leads to unexpected large improvement in thermal conductivity, Nano Letters 16 (6) (2016) 3925–3935, pMID: 27152879. arXiv:http://dx.doi.org/10.1021/acs.nanolett.6b01536, doi:10.1021/acs.nanolett.6b01536.
URL http://dx.doi.org/10.1021/acs.nanolett.6b01536

[15] B. Xiao, Y.-c. Li, X.-f. Yu, J.-b. Cheng, Penta-graphene: A promising anode material as the Li/Na-ion battery with both extremely high theoretical capacity and fast charge discharge rate, ACS Applied Materials & Interfaces 8 (51) (2016) 35342–35352, pMID: 27977126. arXiv:http://dx.doi.org/10.1021/acsami.6b12727, doi:10.1021/acsami.6b12727.
URL http://dx.doi.org/10.1021/acsami.6b12727

[16] R. Krishnan, W.-S. Su, H.-T. Chen, A new carbon allotrope: Penta-graphene as a metal-free catalyst for CO oxidation, Carbon 114 (2017) 465 – 472. doi:https://doi.org/10.1016/j.carbon.2016.12.054.
URL http://www.sciencedirect.com/science/article/pii/S0008622316311290

[17] M.-Q. Le, Mechanical properties of penta-graphene, hydrogenated penta-graphene, and penta-CN2 sheets, Computational Materials Science 136 (2017) 181 – 190. doi:https://doi.org/10.1016/j.commatsci.2017.05.004.

URL http://www.sciencedirect.com/science/article/pii/S0927025617302343

[18] O. Rahaman, B. Mortazavi, A. Dianat, G. Cuniberti, T. Rabczuk, Metamorphosis in carbon network: From penta-graphene to biphenylene under uniaxial tension, FlatChem 1 (2017) 65 – 73. doi:http://dx.doi.org/10.1016/j.flatc.2016.12.001.
URL http://www.sciencedirect.com/science/article/pii/S2452262716300526

[19] Q. Chen, M.-Q. Cheng, K. Yang, W.-Q. Huang, W. Hu, G.-F. Huang, Dispersive and covalent interactions in all-carbon heterostructures consisting of penta-graphene and fullerene: topological effect, Journal of Physics D: Applied Physics 51 (30) (2018) 305301.
URL http://stacks.iop.org/0022-3727/51/i=30/a=305301

[20] R. Krishnan, S.-Y. Wu, H.-T. Chen, Nitrogen-doped penta-graphene as a superior catalytic activity for CO oxidation, Carbon 132 (2018) 257 – 262. doi:https://doi.org/10.1016/j.carbon.2018.02.064.
URL http://www.sciencedirect.com/science/article/pii/S000862231830188X

[21] L. A. Openov, A. I. Podlivaev, On the thermal stability of pentagraphene, JETP Letters 107 (11) (2018) 713–717. doi:10.1134/S0021364018110115.
URL https://doi.org/10.1134/S0021364018110115

[22] J. J. Quijano-Briones, H. N. Fernández-Escamilla, A. Tlahuice-Flores, Doped penta-graphene and hydrogenation of its related structures: a structural and electronic dft-d study, Phys. Chem. Chem. Phys. 18 (2016) 15505–15509. doi:10.1039/C6CP02781D.
URL http://dx.doi.org/10.1039/C6CP02781D

[23] J. Quijano-Briones, H. Fernández-Escamilla, A. Tlahuice-Flores, Chiral penta-graphene nanotubes: Structure, bonding and electronic properties, Computational and Theoretical Chemistry 1108 (2017) 70 – 75.

doi:https://doi.org/10.1016/j.comptc.2017.03.019.
URL http://www.sciencedirect.com/science/article/pii/S2210271X17301238

[24] K. Chenoweth, A. C. T. van Duin, W. A. Goddard, ReaxFF reactive force field for molecular dynamics simulations of hydrocarbon oxidation, The Journal of Physical Chemistry A 112 (5) (2008) 1040–1053. arXiv:http://dx.doi.org/10.1021/jp709896w, doi:10.1021/jp709896w.
URL http://dx.doi.org/10.1021/jp709896w

[25] S. Winczewski, M. Y. Shaheen, J. Rybicki, Interatomic potential suitable for the modeling of penta-graphene: Molecular statics/molecular dynamics studies, Carbon 126 (2018) 165 – 175. doi:https://doi.org/10.1016/j.carbon.2017.10.002.
URL http://www.sciencedirect.com/science/article/pii/S0008622317309958

[26] A. Stukowski, Visualization and analysis of atomistic simulation data with OVITO - the Open Visualization Tool, Modelling and Simulation in Materials Science and Engineering 18 (1) (2010) 015012.
URL http://stacks.iop.org/0965-0393/18/i=1/a=015012

[27] J. Tersoff, Modeling solid-state chemistry: Interatomic potentials for multicomponent systems, Phys. Rev. B 39 (1989) 5566–5568. doi:10.1103/PhysRevB.39.5566.
URL http://link.aps.org/doi/10.1103/PhysRevB.39.5566

[28] J. Tersoff, Erratum: Modeling solid-state chemistry: Interatomic potentials for multicomponent systems, Phys. Rev. B 41 (1990) 3248–3248. doi:10.1103/PhysRevB.41.3248.2.
URL http://link.aps.org/doi/10.1103/PhysRevB.41.3248.2

[29] P. Erhart, K. Albe, Analytical potential for atomistic simulations of silicon, carbon, and silicon carbide, Phys. Rev. B 71 (2005) 035211.

doi:10.1103/PhysRevB.71.035211.
URL http://link.aps.org/doi/10.1103/PhysRevB.71.035211

[30] S. Plimpton, Fast parallel algorithms for short-range molecular dynamics, Journal of Computational Physics 117 (1) (1995) 1 – 19. doi:http://dx.doi.org/10.1006/jcph.1995.1039.
URL http://www.sciencedirect.com/science/article/pii/S002199918571039X

[31] E. Polak, G. Ribiére, Note sur la convergence de méthodes de directions conjuguées, ESAIM: Mathematical Modelling and Numerical Analysis - Modélisation Mathématique et Analyse Numérique 3 (R1) (1969) 35–43.
URL http://eudml.org/doc/193115

[32] J. N. Grima, S. Winczewski, L. Mizzi, M. C. Grech, R. Cauchi, R. Gatt, D. Attard, K. W. Wojciechowski, J. Rybicki, Tailoring graphene to achieve negative Poisson's ratio properties, Advanced Materials 27 (8) 1455–1459. arXiv:https://onlinelibrary.wiley.com/doi/pdf/10.1002/adma.201404106, doi:10.1002/adma.201404106.
URL https://onlinelibrary.wiley.com/doi/abs/10.1002/adma.201404106

[33] M. Parrinello, A. Rahman, Polymorphic transitions in single crystals: A new molecular dynamics method, Journal of Applied Physics 52 (12) (1981) 7182–7190. arXiv:https://doi.org/10.1063/1.328693, doi:10.1063/1.328693.
URL https://doi.org/10.1063/1.328693

[34] S. Nosé, A unified formulation of the constant temperature molecular dynamics methods, The Journal of Chemical Physics 81 (1) (1984) 511–519. arXiv:https://doi.org/10.1063/1.447334, doi:10.1063/1.447334.
URL https://doi.org/10.1063/1.447334

[35] W. G. Hoover, Canonical dynamics: Equilibrium phase-space distributions, Phys. Rev. A 31 (1985) 1695–1697. doi:10.1103/PhysRevA.31.1695.
URL https://link.aps.org/doi/10.1103/PhysRevA.31.1695

[36] G. J. Martyna, D. J. Tobias, M. L. Klein, Constant pressure molecular dynamics algorithms, The Journal of Chemical Physics 101 (5) (1994) 4177–4189. arXiv:https://doi.org/10.1063/1.467468, doi:10.1063/1.467468.
URL https://doi.org/10.1063/1.467468

[37] W. Shinoda, M. Shiga, M. Mikami, Rapid estimation of elastic constants by molecular dynamics simulation under constant stress, Phys. Rev. B 69 (2004) 134103. doi:10.1103/PhysRevB.69.134103.
URL https://link.aps.org/doi/10.1103/PhysRevB.69.134103

[38] M. E. Tuckerman, J. Alejandre, R. López-Rendón, A. L. Jochim, G. J. Martyna, A Liouville-operator derived measure-preserving integrator for molecular dynamics simulations in the isothermal-isobaric ensemble, Journal of Physics A: Mathematical and General 39 (19) (2006) 5629.
URL http://stacks.iop.org/0305-4470/39/i=19/a=S18

[39] A. P. Thompson, S. J. Plimpton, W. Mattson, General formulation of pressure and stress tensor for arbitrary many-body interaction potentials under periodic boundary conditions, The Journal of Chemical Physics 131 (15) (2009) 154107. arXiv:https://doi.org/10.1063/1.3245303, doi:10.1063/1.3245303.
URL https://doi.org/10.1063/1.3245303

[40] S. J. Plimpton, A. P. Thompson, Computational aspects of many-body potentials, MRS Bulletin 37 (5) (2012) 513–521. doi:10.1557/mrs.2012.96.

[41] W. C. Swope, H. C. Andersen, P. H. Berens, K. R. Wilson, A computer simulation method for the calculation of equilibrium constants for the formation of physical clusters of molecules: Application to small water clusters, The Journal of Chemical Physics 76 (1) (1982) 637–649. arXiv:https://doi.org/10.1063/1.442716, doi:10.1063/1.442716.
URL https://doi.org/10.1063/1.442716